G-2 Internal
Version 1.0
July 7, 2020

Run-1 Fast Rotation Analysis with the Cornell Fourier Method

T. Barrett[1], A. Chapelain[1], J. Fagin[1], D. Rubin[1], and D. Seleznev[1]

[1]Cornell University

Abstract

This note presents the reconstruction of the muon beam's radial distribution for each of the Run-1 datasets using the Cornell fast rotation Fourier method. The radial distribution is used to estimate the electric field correction to the muons' anomalous spin precession frequency ω_a.

Contents

1 Introduction

This note presents the reconstruction of the radial distribution of the muon beam for Run-1 of the Fermilab E–989 Muon $g-2$ Experiment using the Cornell fast rotation Fourier method. The details of the Cornell fast rotation Fourier analysis are presented in [1] and the study of its performance with toy Monte Carlo simulations presented in [2]. More details about the Cornell fast rotation Fourier method can be found in [3, 4]. The analysis code's user guide can be found in [5]. The fast rotation Fourier method aims at reconstructing the radial distribution of the stored muon beam, via reconstructing the frequency distribution, in order to estimate the electric field correction C_E to the anomalous spin precession frequency of the muon ω_a. The electric field correction can be estimated in first approximation with the following formula:

$$C_E = \frac{\Delta\omega_a}{\omega_a} = -2n(1-n)\beta^2 \frac{\langle x_e^2 \rangle}{R_0^2}, \tag{1}$$

where

$$\langle x_e^2 \rangle = x_e^2 + \sigma^2, \tag{2}$$

where x_e is the equilibrium radius (average radial position) and σ the radial width of the beam, R_0 is the magic radius of 7112 mm, β the relativistic speed, and n the field index that relates to the electrostatic quadrupole electric field gradient as

$$n = \frac{m\gamma r}{pB_0}\frac{\partial E_r}{\partial r}, \tag{3}$$

where m is the mass, γ the Lorentz factor, r the radial distance from the center of the storage ring, p the momentum, and E_r the radial component of the quadrupole electric field.

The ultimate goal of the Fermilab E–989 experiment is an uncertainty budget on the electric field correction of 20 ppb. This uncertainty translates into knowing both the average and the width of the cyclotron revolution frequency distribution within a few 0.1 kHz, which corresponds to knowing both the equilibrium radius and the width of the radial distribution within a few 0.1 mm. The electric field correction uncertainty budget for Run-1 is not as stringent given the anticipated statistical and systematic uncertainties on ω_a of hundreds of ppb. A total uncertainty of 50 ppb on the electric field correction for Run-1 would reach enough precision.

The reader is expected to be familiar with [1] and [2] before reading further.

2 Datasets

The datasets analyzed in this note include the 60Hour, 9Day, EndGame, and HighKick datasets from Run-1. The versions of the reconstructed data used in this analysis and provided by the production team are [6]:

`gm2pro_daq_full_run1_60h_5039A_GLdocDB16021-v2`
`gm2pro_daq_full_run1_9d_5040A_GLdocDB17018-v3`
`gm2pro_daq_full_run1_EndGame_5042B_GLdocDB20839-v1`
`gm2pro_daq_full_run1_HighKick_5042B_GLdocDB20949-v3`

The full data quality (fill-by-fill, subrun-by-subrun including the magnetic field information) is applied. The relevant information to the fast rotation analysis is obtained from the Recon West data products.

3 Fast Rotation signal

The details regarding how to produce the fast rotation signal can be found in [1] Sec. 3.

3.1 Positron counts histogram

The input to the fast rotation analysis is the same as the input to the anomalous spin precession frequency analysis: a histogram of the positron counts versus the time into the fill. For each of the four Run-1 datasets, this histogram was produced for each of the 24 calorimeters, for each of the 8 bunches in the accelerator cycle, and for each run number. The nominal value of the positron energy threshold is 1500 MeV. The choice of the energy threshold will be a source of systematic uncertainty (see Sec. 7.7).

3.2 Combination of the 24 calorimeters

The positron counts of the 24 calorimeters are merged together for the nominal analysis. The histograms from calorimeters #2 to #24 are added to the histogram of calorimeter #1 (taken arbitrarily as the reference), time-shifting them by $(\# - 1) \times T_c/24$, where # is the calorimeter number and T_c the nominal cyclotron period of

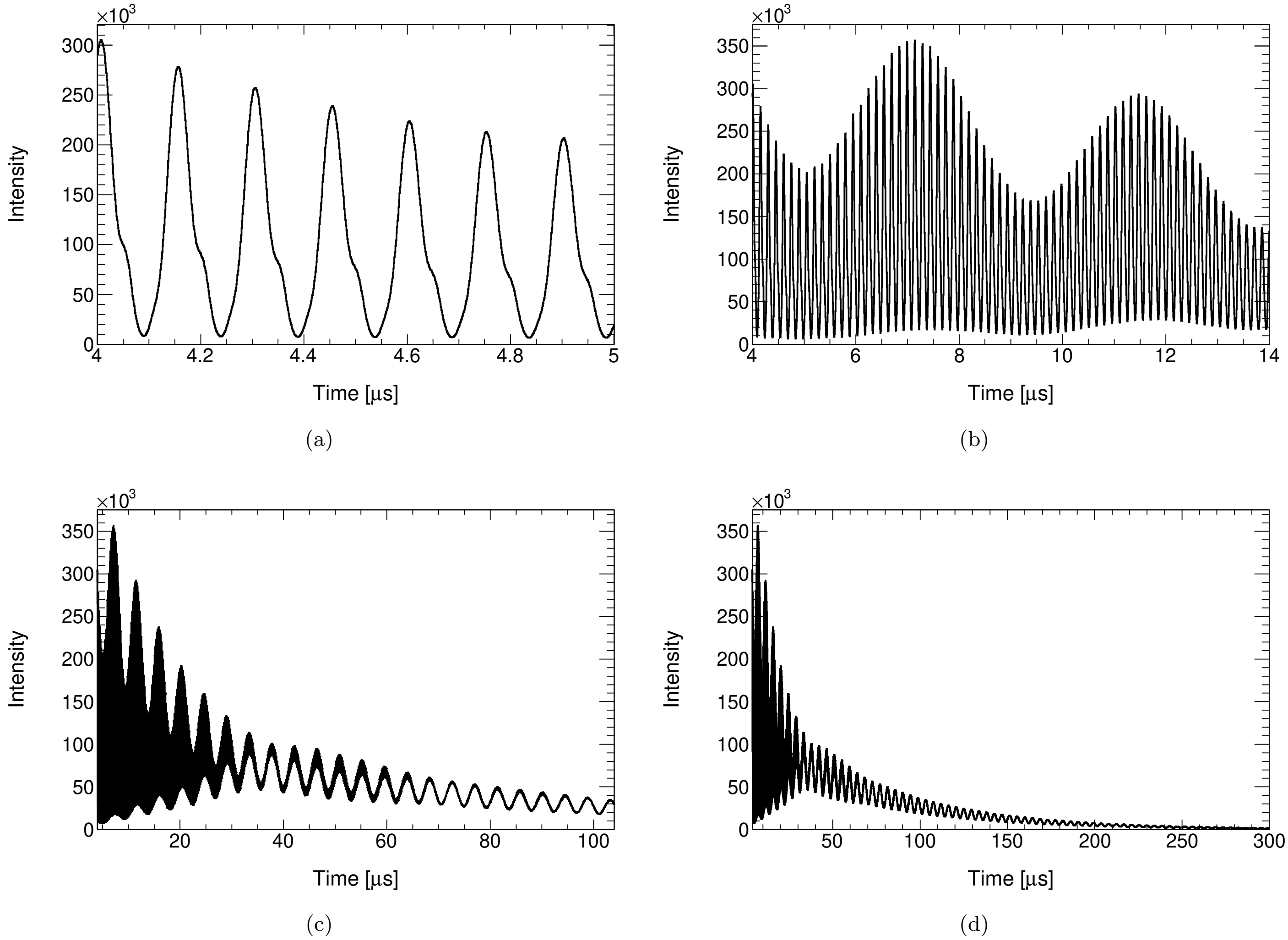

Figure 1: Positron counts as a function of time as seen by all the calorimeters combined in the Run-1 EndGame dataset, for the following time ranges: (a) 4–5, (b) 4–14, (d) 4–104, and (e) 4–300 μs with respect to the beam injection. The time interval is 1 ns.

149.14 ns corresponding to the so-called "magic momentum". The value of the cyclotron period is updated to the measured value after completing the first round of the analysis and the analysis is performed again. The small variation of the cyclotron frequency results in a small variation of the time-shift constant (well below the ns-level) and therefore yields a negligible change in the fast rotation results. Figure 1 shows the positron counts histogram for all the 24 calorimeters combined, using the EndGame dataset as a representative example. The time interval of the histogram is 1 ns. The analysis is also performed per calorimeter, per bunch, and per run as presented in 5.

3.3 Wiggle fit

It is necessary to fit the positron counts histogram in order to divide out the exponential decay of the muon population (at the very least). Section 7.6 will show that the results change little when fitting for more than the muon life-time (i.e. ω_a and ω_{cbo}). The default fit is the 9-parameter fit that includes the muon lifetime, anomalous spin precession, and CBO modulation:

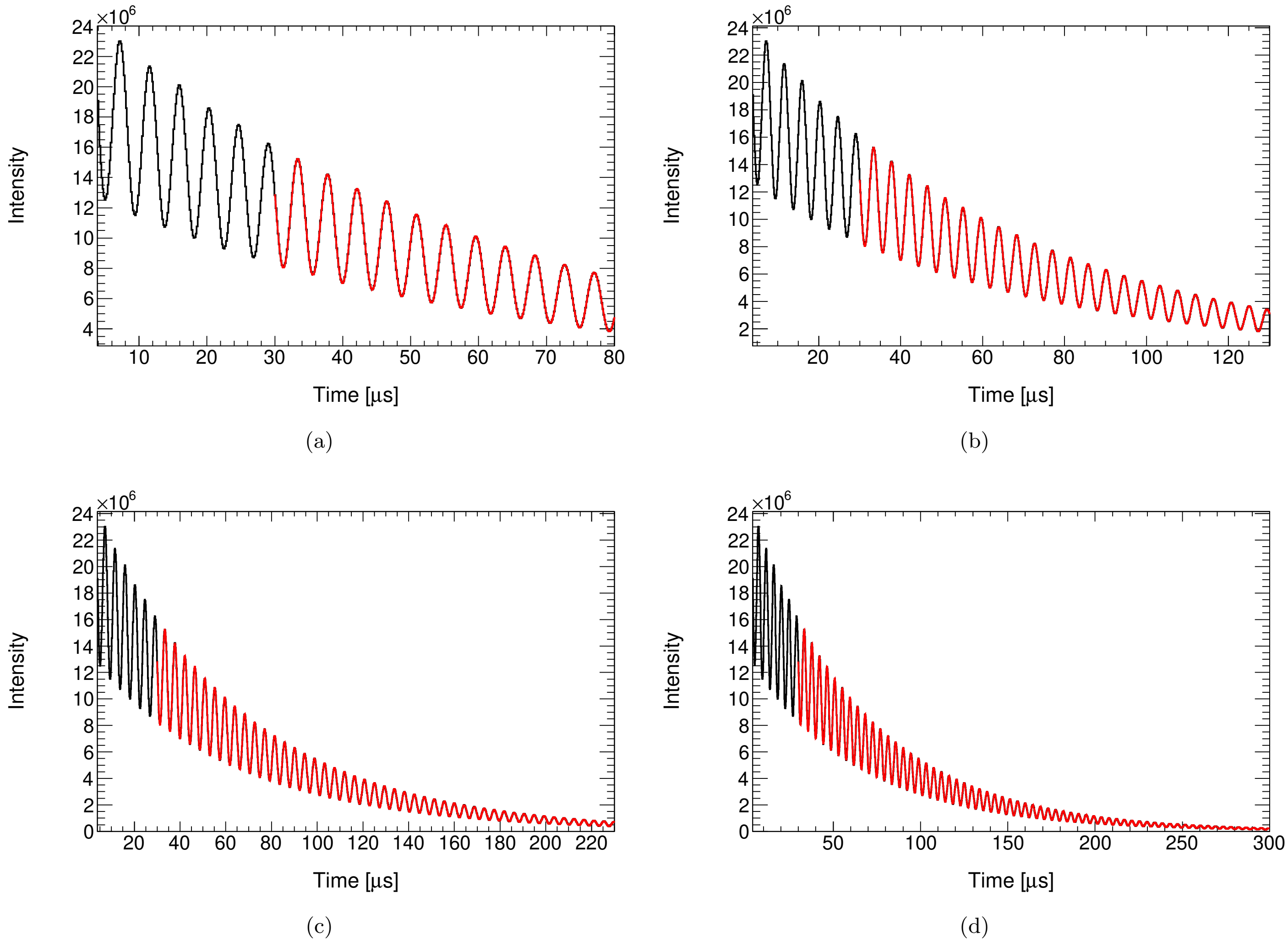

Figure 2: 9-parameter fit of the positron counts histogram as a function of time as seen by all the calorimeters combined in the Run-1 EndGame dataset, for the following time ranges: (a) 4–80, (b) 4–130, (d) 4–230, and (e) 4–300 μs with respect to the beam injection. The time interval is 149 ns.

$$N(t) = N_0 \cdot e^{-t/\tau_\mu}[1 + A \cdot cos(\omega_a t + \phi)] \cdot e^{-t/\tau_{cbo}}[1 + A_{cbo} \cdot cos(\omega_{cbo} t + \phi_{cbo})], \quad (4)$$

where N_0 is the number of detected positron at $t = 0$, τ_μ is the boosted muon lifetime of about 64 μs, A (called the asymmetry) is the amplitude of the anomalous spin precession modulation, ω_a the anomalous spin precession frequency (or spin tune), ϕ the phase of the modulation, τ_{cbo} the CBO lifetime, A_{cbo} the amplitude of the CBO modulation, ω_{cbo} the frequency of the CBO modulation, and ϕ_{cbo} the phase of the CBO modulation.

Figure 2 shows the 9-parameter fit of the positron counts histogram for the EndGame dataset starting at 30 μs with respect to the beam injection. The histogram was re-binned to a time interval of 149 ns in order to average out the fast rotation of the muon bunch. Appendix **??** shows the fit residuals for different time ranges.

3.4 Fast rotation signal

The fast rotation signal is obtained by dividing out the fit function from the original positron counts histogram, given the proper normalization to account for the 1-ns versus 149-ns time intervals. Figure 3 shows the fast rotation signal from the Run-1 EndGame dataset for different time ranges. The appendices **??** and **??** show the various fast rotation histograms for each calorimeter and each bunch.

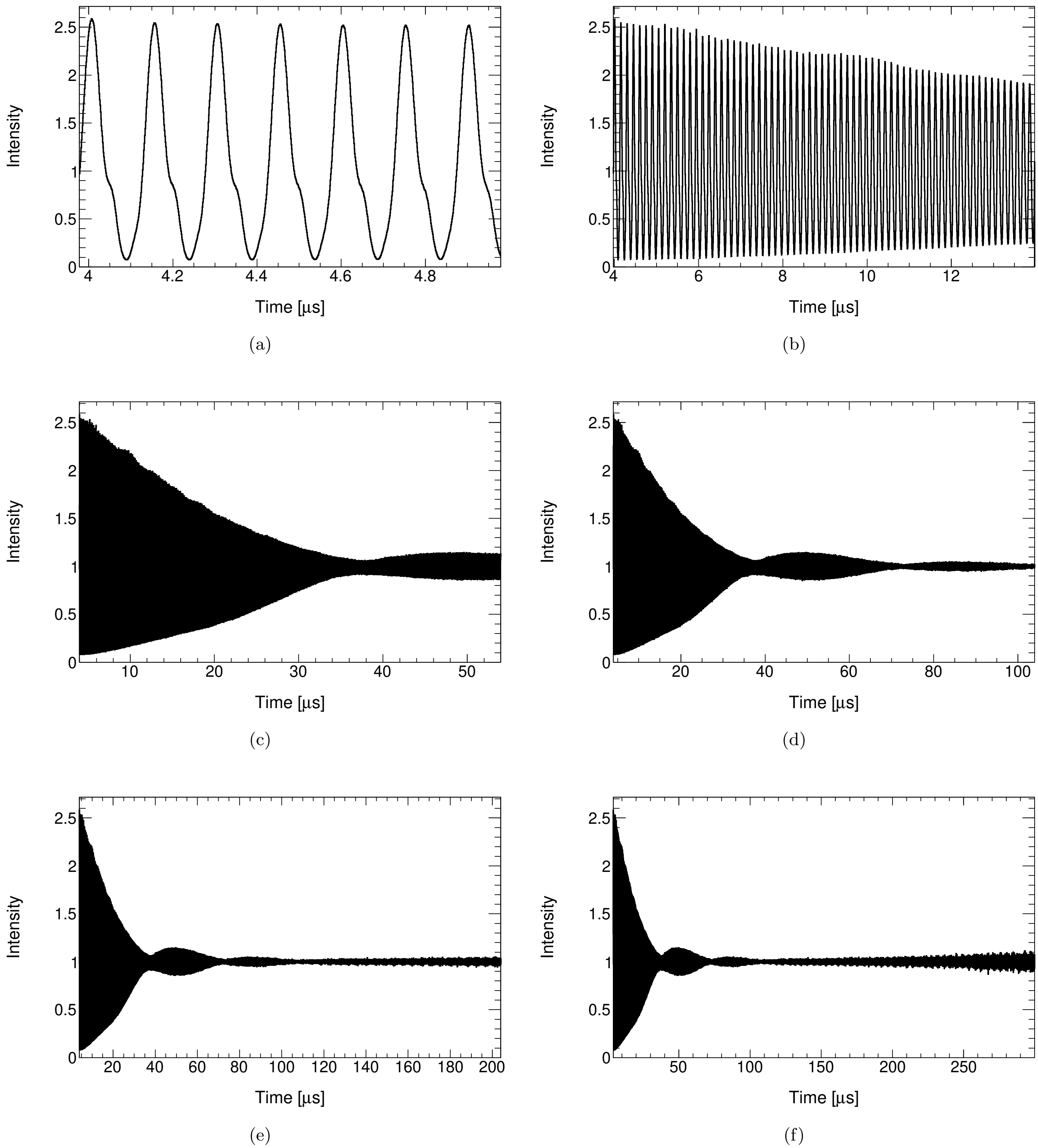

Figure 3: Fast rotation signal as a function of time as seen by all the calorimeters combined in the Run-1 EndGame dataset, for the following time ranges: (a) 4–5, (b) 4–14, (d) 4–54, (e) 4–104, (f) 4–204, and (g) 4–300 μs with respect to the beam injection. The time interval is 1 ns. The modulation with a 35 μs period corresponds to the beam partially and slowly re-bunching due to its asymmetric momentum distribution.

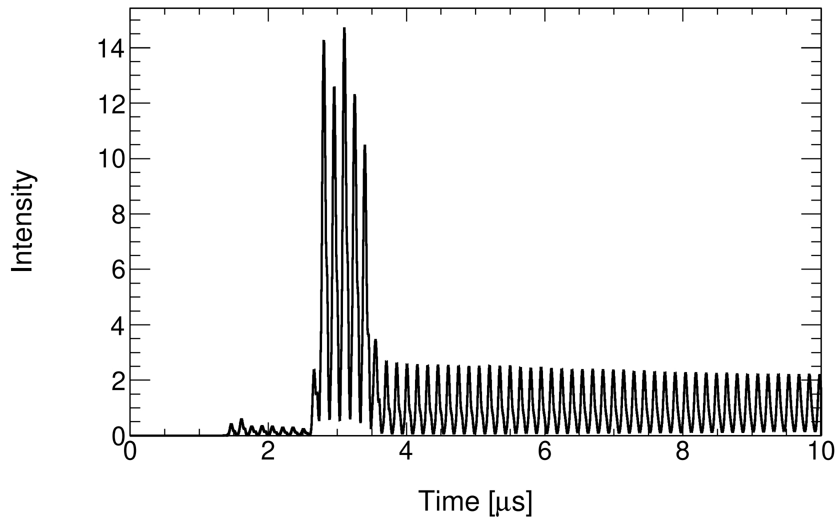

Figure 4: Fast rotation signal as a function of time as seen by all the calorimeters combined in the Run–1 EndGame dataset, between 0 – 10 μs after beam injection. The time interval is 1 ns.

4 Nominal analysis

This section will detail the nominal analysis of the Run–1 datasets. Section 6 and 7 will present respectively the statistical and systematic uncertainties estimation. The details of the analysis can be found in [1].

4.1 Choice of the Start Time (t_s) Parameter

The t_s parameter is the start time of the analysis. The ideal case would be $t_s = t_0$, where t_0 corresponds to the time when the centroid of the longitudinal beam profile is detected by calorimeter #1 on the first turn after injection. This is ideal because the Fourier analysis method uses a cosine transform, which implicitly takes an even extension of the fast rotation signal, mirrored about the time t_0. Therefore, if we can supply the signal from $t_s = t_0$ onward, the cosine transform has all of the data it needs to mirror the signal appropriately. Unfortunately, this ideal scenario is not possible for two reasons. The first is the saturation of the calorimeter electronics during the first μs of the fill due to the high intensity of the incoming beam. The second is the presence of contamination in the muon beam due to beam-line positrons. The positrons are lost due to synchrotron radiation after about 3–4 μs. Figure 4 shows the fast rotation signal from the EndGame dataset for the first 10 μs. The first μs is not available due to the saturation, and the signal stabilizes at 3–4 μs after the positrons are lost. The t_s value, because of the reasons explained above, is set to $t_s = 4$ μs. This value is slightly optimized such that t_s corresponds to a normalized intensity of 1 in the fast rotation signal. This is done in order to minimize the effects of spectral leakage (see [1] Sec. 7.1 and 7.2). The optimized start times used in the nominal analysis for each dataset are tabulated in Table 1.

Dataset	t_0 (ns)	t_s (μs)	t_m (μs)
60Hour	121.65	3.9725	299.9665
9Day	128.03	3.9775	300.0665
EndGame	129.27	3.9785	299.9915
HighKick	127.23	3.9755	300.0925

Table 1: Time parameters used in the nominal cosine transform for each of the Run–1 datasets. t_0 is the centroid of the first turn after injection (aligned to Calorimeter #1), t_s is the start time of the cosine transform, and t_m is the end time.

4.2 Choice of the End Time (t_m) Parameter

The t_m parameter is the end time of the analysis. The nominal choice for each dataset is $t_m = 300$ μs. This value is optimized by performing a t_m scan (see Sec. 7.3). As explained in [1] Sec. 7.3 and in [2] Sec. 4.3, when increasing the length of the fast rotation signal there is a trade-off between improving the frequency resolution and adding exponentially growing statistical noise at late time. The t_m scan allows us to optimize this trade-off, by selecting the latest value for which the results of the analysis appear stable. The exact value of t_m is optimized further in the same fashion as t_s, such that the intensities match at both t_s and t_m. The optimized end times used in the nominal analysis for each dataset are tabulated in Table 1.

4.3 Choice of the t_0 parameter

The t_0 parameter corresponds to the time when the centroid of the longitudinal profile of the beam is detected by calorimeter #1 on the first turn after injection. Given the saturation and the beam-line positron contamination, the data corresponding to the first turn is not recorded. The t_0 value therefore needs to be extrapolated and optimized. The iterative optimization procedure is explained in [1] Sec. 6. It relies on a χ^2-minimization fitting for the "background" of the cosine transform of the fast rotation signal. This background consists of side lobes introduced by the non-ideal choice of $t_s > t_0$, which is effectively a rectangular windowing of the data. The iterative procedure begins by fitting the outermost data points of the frequency distribution, which correspond to unphysical cyclotron frequencies beyond the range allowed by the collimators. On subsequent iterations, the fit range moves inward toward the central peak, including more data points whose fit residuals are within a few standard deviations, based on the set of residuals from the previous iteration. (This choice, referred to as the "background definition threshold," is studied later in this note as a systematic uncertainty.) Figure 5 shows the results of four iterations: the optimum background fit for each iteration and the χ^2 distribution of the background fit as a function of t_0. After the fourth iteration, the optimized t_0 values for each dataset are tabulated in Table 1. These values are consistent with the work presented in [7]. Figure 6 shows the optimum background fit after the t_0 optimization procedure.

4.4 Frequency distribution

Once the t_0 optimization is performed, the optimum cosine Fourier transform is available. Its background side lobes are removed by subtracting the background fit. After this subtraction is performed, the fit residuals still remain as noise along the edges of the distribution, including the frequency ranges vetoed by the collimators. To ensure this

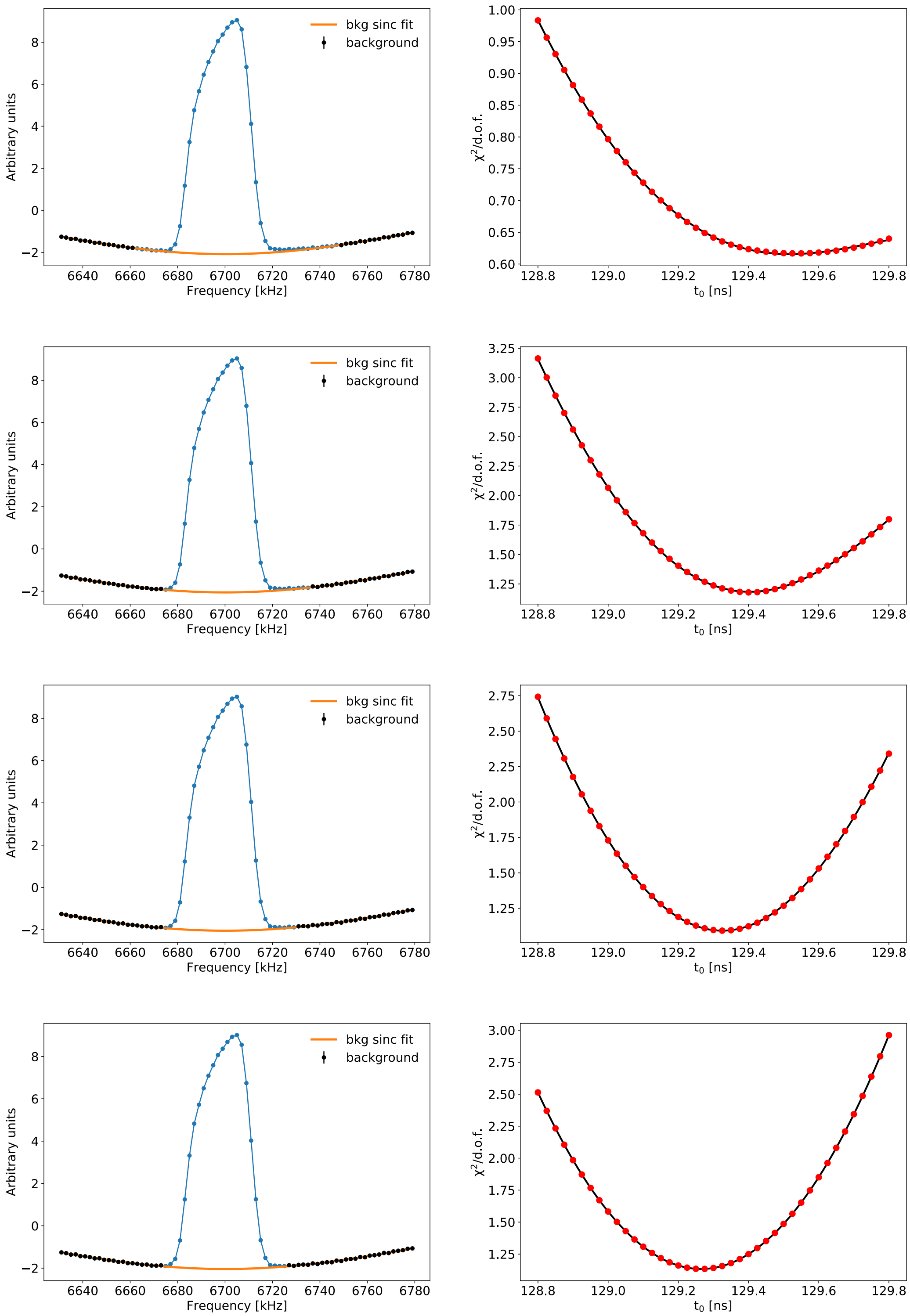

Figure 5: Results of the four iterations (from top to bottom) of the t_0 optimization procedure for the Run–1 EndGame dataset. The figures on the left show the cosine Fourier transform at each iteration, including the cardinal sine background fit for the optimum t_0 value. Notice the fit definition moving inward with each step, which is the purpose of the iterative procedure. The figures on the right show the χ^2 distribution of the background fit as a function of t_0.

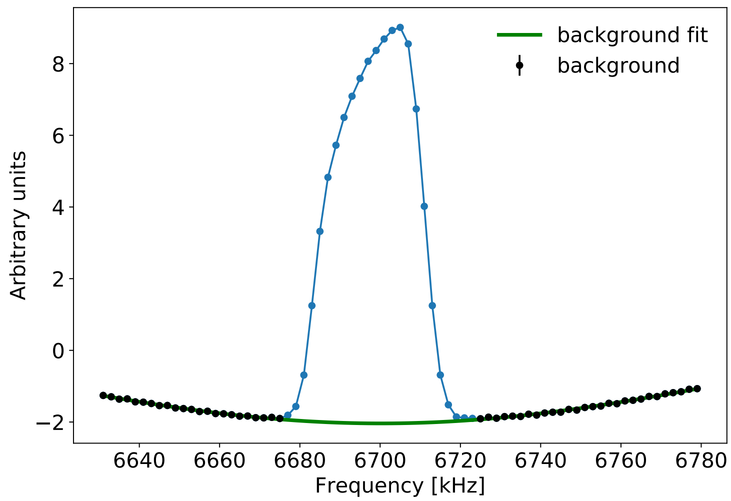

Figure 6: Optimum cardinal sine background fit to the cosine Fourier transform for the Run–1 EndGame dataset.

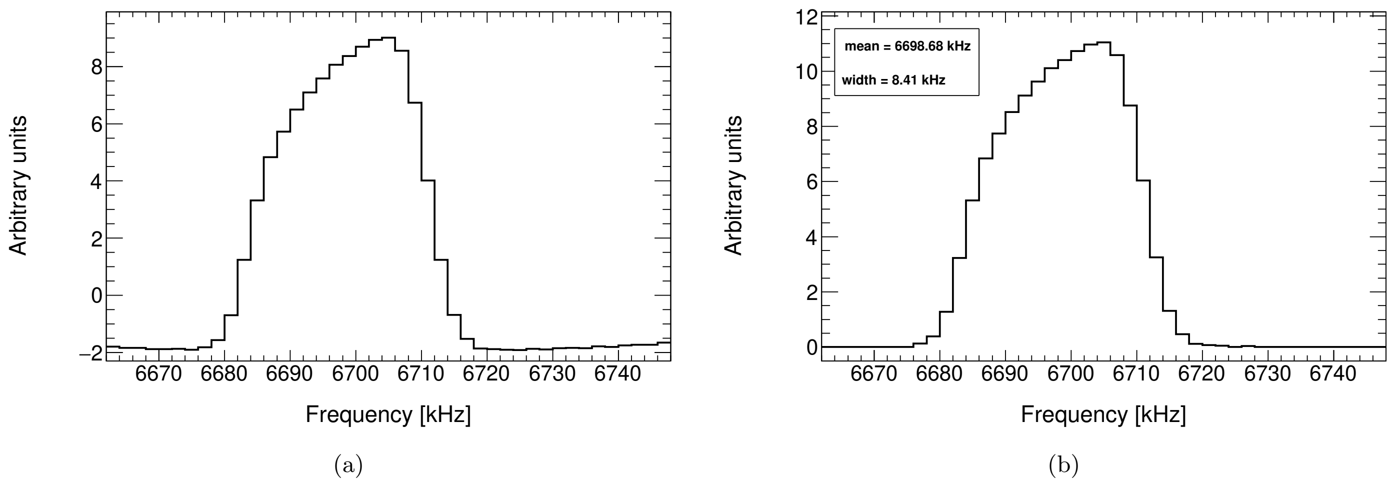

Figure 7: Frequency distributions from the Run–1 EndGame dataset: (a) cosine Fourier transform, and (b) corrected cosine Fourier transform, limited to the range allowed by the collimator aperture.

unphysical noise does not bias the determination of the distribution's mean and width, any frequency bins whose heights are within a few standard deviations from zero are flattened. (This functions much like the background definition threshold, but the choice is independent, and is treated as a separate "background removal threshold" systematic uncertainty.) Figure 7 shows the cosine Fourier transform before and after background subtraction for the EndGame dataset, limited to the range allowed by the collimator aperture. The measured averages and widths of the cyclotron frequency distributions are tabulated in Table 2 for each of the Run–1 datasets.

4.5 Radial distribution

The distribution of cyclotron frequencies can be converted to the distribution of cyclotron radii as explained in [1], Sec. 8. Figure 8 shows the radial distribution corresponding to 7 in beam coordinates, limited to the range allowed

Dataset	$\langle f_c \rangle$ (kHz)	σ_f (kHz)
60Hour	6699.23	8.65
9Day	6699.00	8.70
EndGame	6698.68	8.41
HighKick	6700.36	8.67

Table 2: Mean cyclotron frequencies $\langle f_c \rangle$ and standard deviations σ_f recovered from the nominal cosine transform for each of the Run–1 datasets.

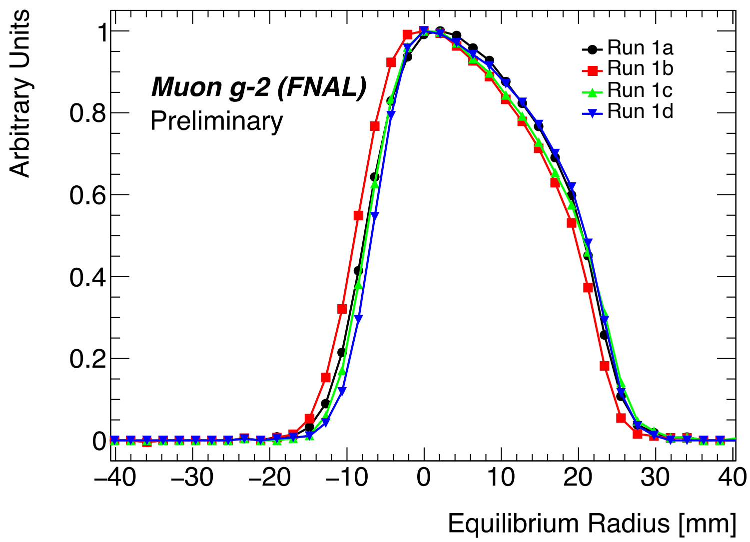

Figure 8: Radial distribution in beam coordinates for the four Run–1 datasets, limited to the range allowed by the collimator aperture.

Dataset	$\langle x_e \rangle$ (mm)	σ (mm)
60Hour	6.09	9.19
9Day	6.34	9.24
EndGame	6.67	8.94
HighKick	4.89	9.21

Table 3: Mean equilibrium radii $\langle x_e \rangle$ and standard deviations σ (in beam coordinates) recovered from the nominal cosine transform for each of the Run–1 datasets.

by the collimator aperture (± 45 mm). These coordinates are radial offsets from the magic radius, such that $x = 0$ corresponds to 7112 mm from the center of the ring, and positive (negative) values correspond to radially outward (inward) positions. The recovered mean equilibrium radii and widths are tabulated in Table **??** for each of the Run–1 datasets.

Dataset	f_{cbo} (kHz)	n	C_E (ppb)
60Hour	370.44	0.1075	-461
9Day	413.64	0.1197	-523
EndGame	367.05	0.1066	-468
HighKick	414.29	0.1198	-453

Table 4: Recovered CBO frequencies f_{cbo}, field indices n, and electric field corrections C_E for each of the Run–1 datasets.

4.6 Electric field correction estimation

The electric field corrections are estimated using Eq. (1), given the radial distributions in Fig. 8. The field index in Eq. (1) is expressed (in the continuous quad approximation) as

$$n = 1 - \nu_x^2, \tag{5}$$

where ν_x is the radial tune,

$$\nu_x = 1 - f_{\text{cbo}}/f_c, \tag{6}$$

where f_{cbo} is the CBO frequency extracted from the 9-parameter wiggle fit and f_c is the average cyclotron frequency. These results are tabulated in Table **??** for each of the Run–1 datasets. The n values are in very good agreement with the field index measurements done by the tracker and calorimeter teams.

Dataset	Per-Calo Fit (ns)	$\langle T_c \rangle/24$ (ns)
60Hour	6.214(3)	6.220
9Day	6.217(3)	6.220
EndGame	6.218(2)	6.220
HighKick	6.212(4)	6.219

Table 5: Calorimeter time alignment constants. The first column results from a linear fit to the optimized t_0 per-calorimeter. The second column uses the measured average cyclotron period $\langle T_c \rangle = 1/\langle f_c \rangle$ from the combined analysis. The numbers in () denote uncertainties in the last digit.

5 Analysis by Calorimeter, Bunch, and Run Numbers

This section will detail the fast rotation analysis performed per-calorimeter, per-bunch, and per-run.

5.1 Per-calorimeter analysis

The results presented in Sec. 4 correspond to all the 24 calorimeters combined, i.e. the results correspond to azimuthal averaging around the ring. It is important to perform the analysis per-calorimeter to ensure the results are consistent all around the ring. Any significant difference would have to be understood and, if needed, included in the anomalous spin precession analysis. The per-calorimeter fast rotation analysis is almost identical to the nominal analysis performed on all the calorimeters combined. The only difference is that the set of data points used for the background fit in the frequency domain is fixed to the selection from the nominal analysis. Using the iterative method described previously, different statistical fluctuations could cause the method to converge on different background definitions for each calorimeter, which would bias the determination of t_0 and the overall corrected frequency distribution. Using this fixed background definition, the t_0 parameter is optimized for each calorimeter. Figure 9 shows the optimized t_0 values as a function of calorimeter number for each of the Run–1 datasets.

It is expected to change by $T_c/24$ between each successive calorimeter, where T_c is the average cyclotron revolution period. For instance, the magic cyclotron period of 149.14 ns corresponds to a time shift of 6.214 ns between two consecutive calorimeters. The calorimeter time alignment constants from the per-calorimeter t_0 fit results are tabulated in Table 5, along with the time alignment constants computed from each dataset's average cyclotron period $\langle T_c \rangle$. The per-calorimeter fit results differ from $\langle T_c \rangle/24$ by between $1 - 2$ standard deviations across all four datasets, showing fair statistical agreement between the two methods.

Figure 10 shows the radial distributions for all 24 calorimeters overlaid. The visual agreement for each dataset is satisfying. Fig. 11 shows x_e, σ and C_E as a function of calorimeter number. Weighting each calorimeter by its statistics, the per-calorimeter averages and standard deviations are tabulated in Table 6. These averages show good agreement with the results presented previously for all the calorimeters combined.

The error bars in Fig. 11 are the statistical uncertainties, scaled from the nominal statistical uncertainty analysis by $\sqrt{N_{\text{dataset}}/N_{\text{calo}}}$, where N is the number of hits. Most of the per-calorimeter results are statistically in reasonable agreement, with some pairwise differences on the order of 4 standard deviations[1]. The spread in

[1] The systematic uncertainty is expected to be larger than the statistical uncertainty but is not estimated per-calorimeter.

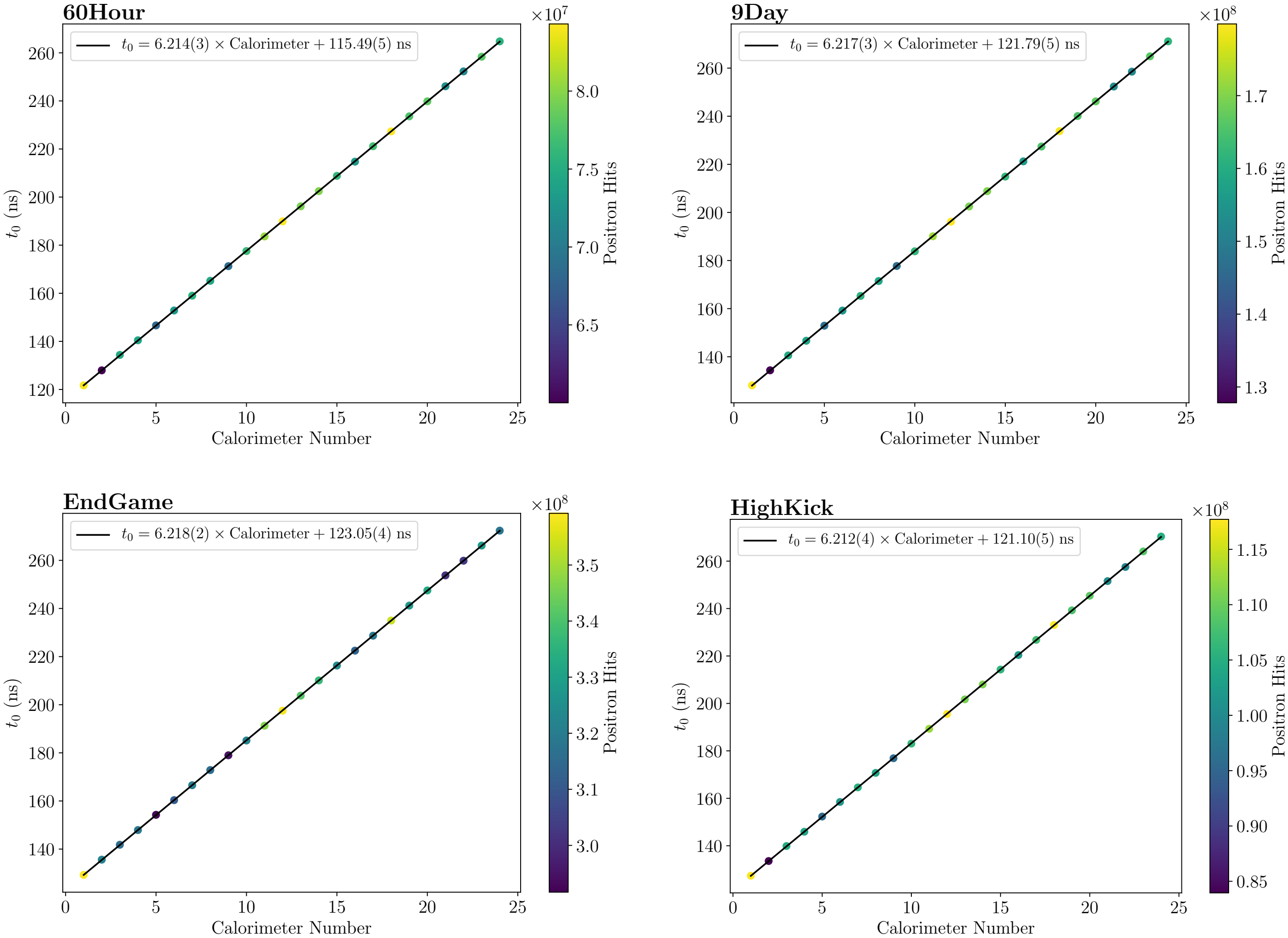

Figure 9: Optimized t_0 values as a function of calorimeter number for each of the four Run–1 datasets. The black line is a linear fit to the data points; the number in () is the uncertainty associated with the last digit. The statistical uncertainty on each data point (see Sec. **??**) is about 0.055 ns and thus is too small to be seen here.

Dataset	x_e (mm)		σ (mm)		C_E (ppb)	
	mean	width	mean	width	mean	width
60Hour	6.10	0.079	9.16	0.067	−459	6.30
9Day	6.37	0.108	9.18	0.048	−520	7.29
EndGame	6.70	0.071	8.90	0.035	−467	3.87
HighKick	4.86	0.107	9.18	0.048	−450	6.94

Table 6: Statistics-weighted per-calorimeter averages and standard deviations for the equilibrium radius x_e, radial width σ, and e-field correction C_E.

C_E, for example, is roughly between one and two times the expected statistical uncertainty for each dataset. This indicates the presence of some non-statistical effect in the per-calorimeter analysis[2].

[2]In the presence of purely statistical effects, the results and associated uncertainties should be the same when performing the analysis on the combined inputs or when combining the outputs of the individual analyses.

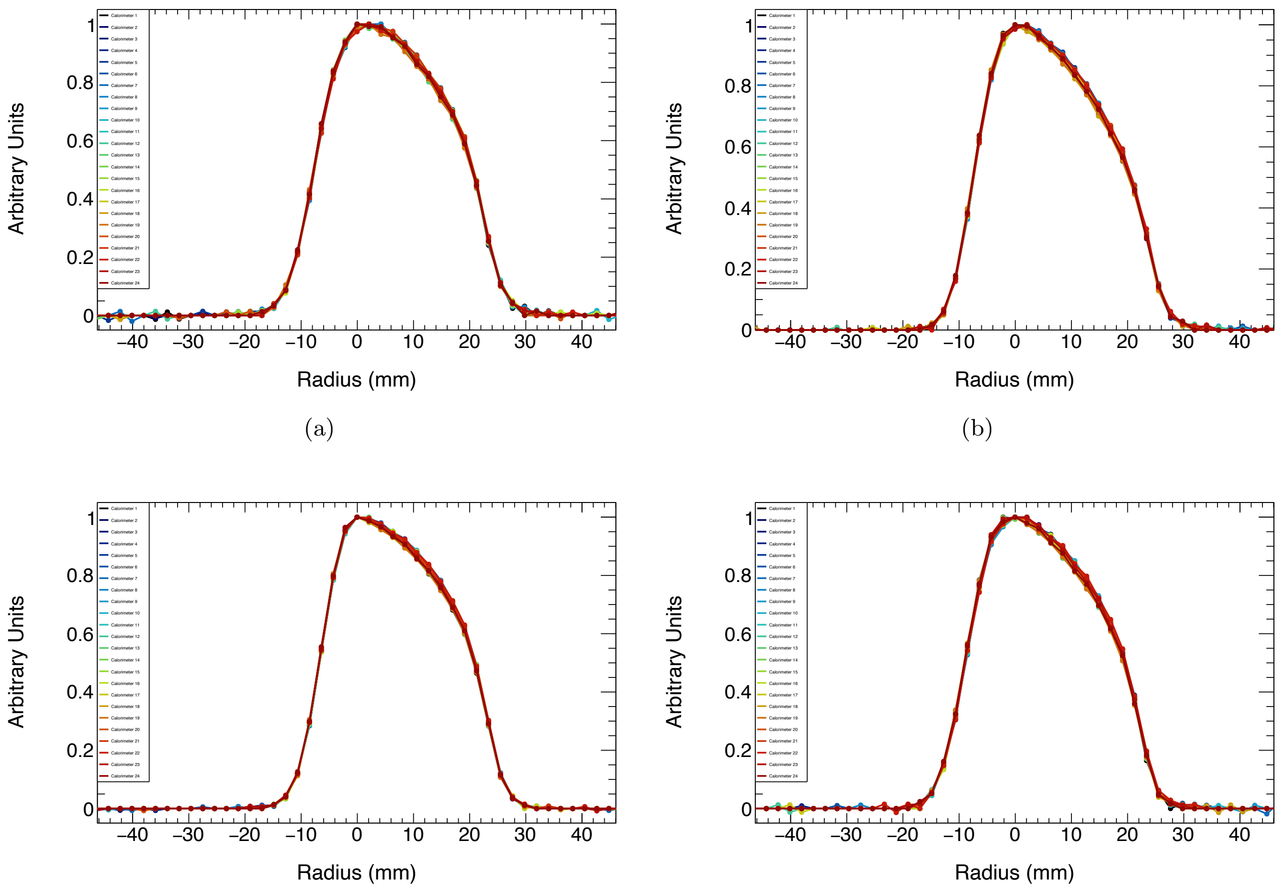

(c) (d)

Figure 10: Radial distributions for all 24 calorimeters overlaid: (a) 60Hour, (b) 9Day, (c) EndGame, (d) HighKick.

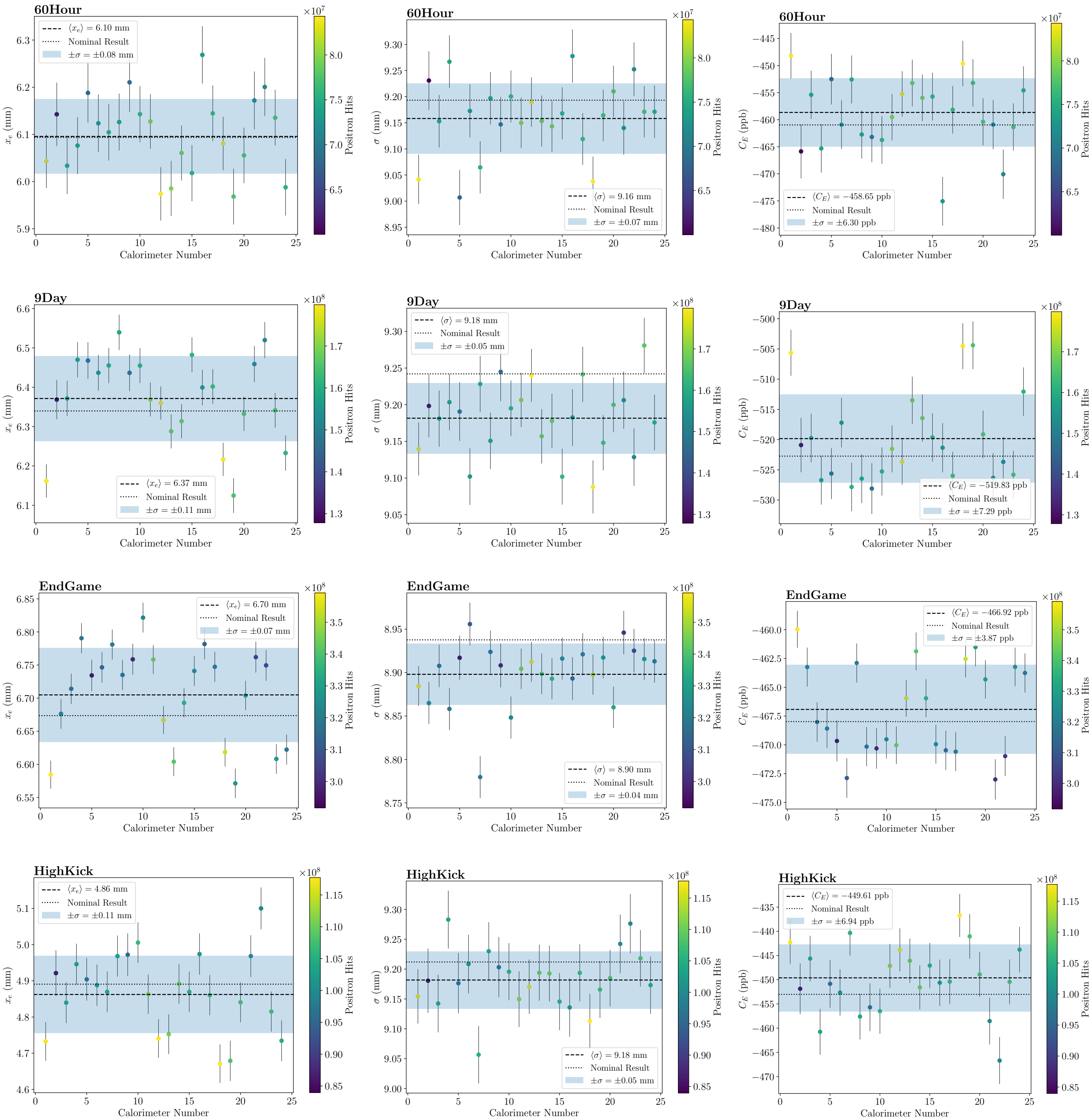

Figure 11: Results of the fast rotation analysis per-calorimeter. The error bars show the statistical uncertainty (see Sec. 6).

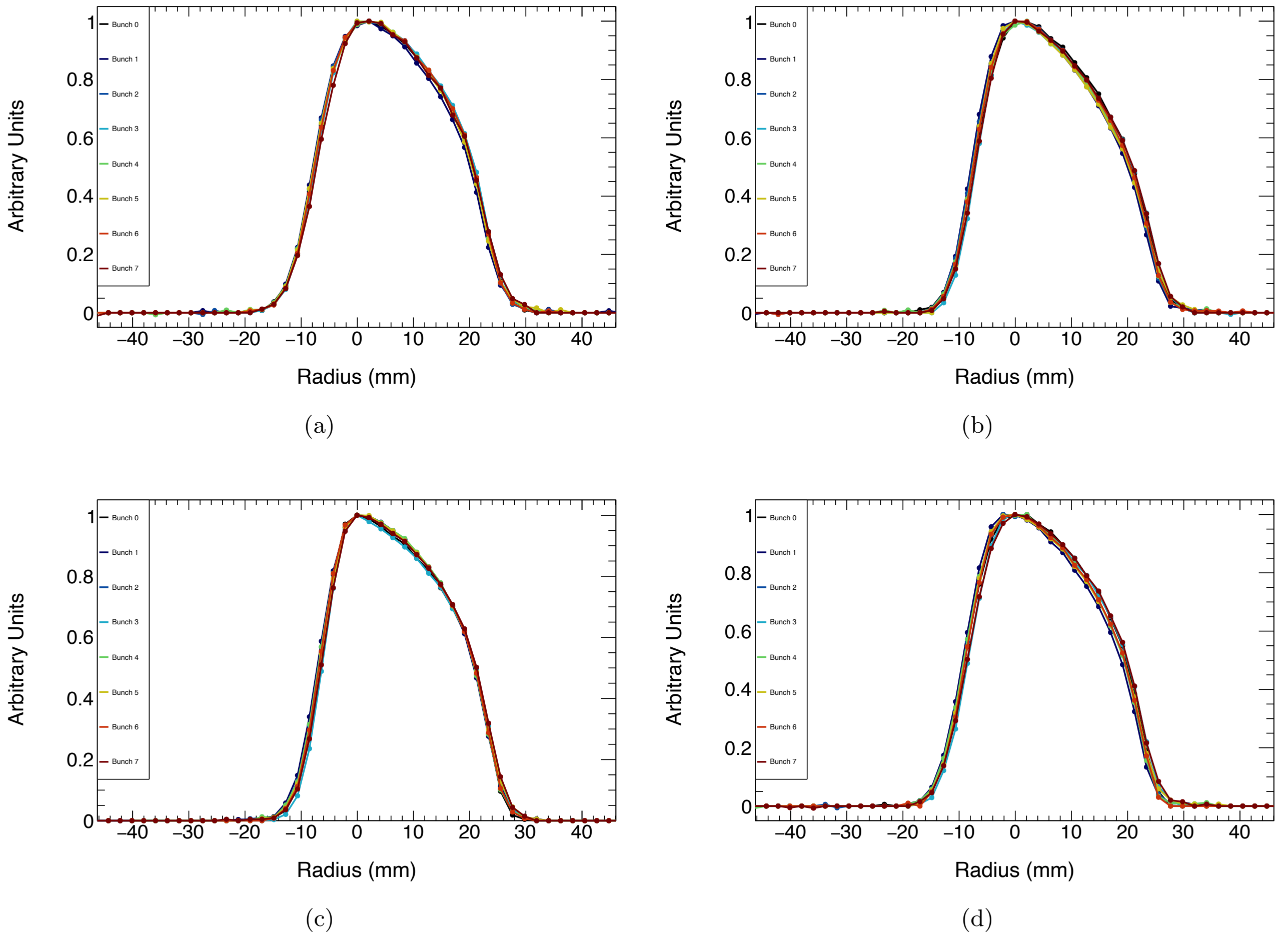

Figure 12: Radial distributions for all 8 bunches overlaid: (a) 60Hour, (b) 9Day, (c) EndGame, (d) HighKick.

5.2 Per-bunch analysis

Figure **??** in App. **??** shows that the 8 bunches in the accelerator cycle have different longitudinal profiles. Given that the length of the incoming pulse is about 200 ns, and that the kick provided by the three kickers inside the ring is inhomogeneous over time, one can expect different stored radial distributions for each bunch. It is therefore interesting to look at the fast rotation results for each bunch individually[3]. As in the per-calorimeter analysis, the set of data points used for the background fit is fixed to the set identified by the nominal analysis. Not fixing the background definition would introduce a systematic bias in the per-bunch results, making the results across bunches more difficult to compare. The t_0 parameter is optimized for each bunch and is expected to be randomly distributed because of the differences in the beam profiles (i.e. the time centroid of each bunch's injection profile depends on the profile's shape).

Figure 12 shows the radial distributions for all 8 bunches overlaid.

Fig. 13 shows C_E as a function of bunch number. The error bars are the statistical uncertainties, scaled from the nominal statistical uncertainty analysis by $\sqrt{N_{\text{dataset}}/N_{\text{bunch}}}$, where N is the number of hits. Weighting each bunch by its statistics, the averaging of them all yields the results in Table 7, which are in good agreement with

[3]The anomalous spin precession frequency is nominally performed by combining all the bunches together.

Dataset	t_0 (ns)		x_e (mm)		σ (mm)		C_E (ppb)	
	mean	width	mean	width	mean	width	mean	width
60Hour	121.57	7.34	6.09	0.17	9.20	0.04	-461	6.40
9Day	127.30	8.19	6.29	0.26	9.15	0.06	-513	14.26
EndGame	128.74	6.22	6.68	0.19	8.89	0.07	-465	9.47
HighKick	126.45	7.62	4.85	0.32	9.15	0.06	-447	12.90

Table 7: Statistics-weighted per-bunch averages and one-sigma spreads for the recovered t_0, equilibrium radius x_e, radial width σ, and e-field correction C_E.

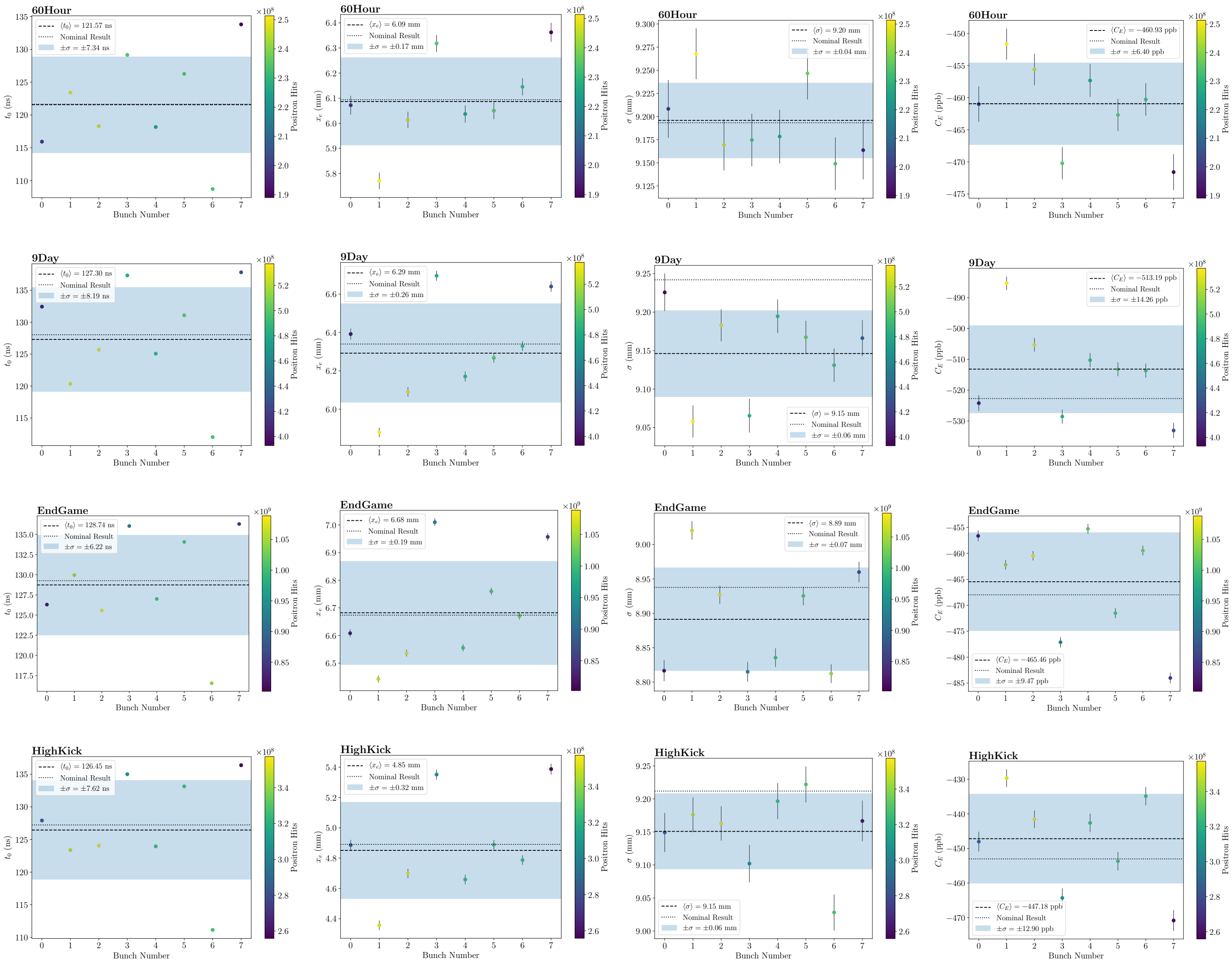

Figure 13: Per-bunch results from the fast rotation analysis. Error bars show statistical uncertainty (see Sec. 6).

the results presented previously for all the calorimeters and bunches combined. This indicates that the per-bunch and per-calorimeter information may be linearly combined before or after performing the fast rotation analysis.

Dataset	t_0 (ns)		x_e (mm)		σ (mm)		C_E (ppb)	
	mean	width	mean	width	mean	width	mean	width
60Hour	121.66	1.03	6.08	0.11	9.16	0.09	−459	7.31
9Day	128.03	1.05	6.33	0.22	9.17	0.10	−516	15.04
EndGame	129.30	1.67	6.69	0.11	8.87	0.13	−465	8.11
HighKick	127.36	3.42	4.87	0.46	9.16	0.11	−449	22.31

Table 8: Statistics-weighted per-run averages and one-sigma spreads for the recovered t_0, equilibrium radius x_e, radial width σ, and e-field correction C_E.

5.3 Per-run analysis

Within each dataset, measurements are typically broken up temporally into "runs" and "sub-runs." The nominal analysis uses the data from all runs combined. However, the operating performance of many experimental subsystems (e.g. kickers, quads, etc.) can vary over time throughout the dataset. This means it is important to study the results of the analysis as a function of run number, in order to evaluate the stability of the results over the extent of the dataset.

As in the per-calorimeter and per-bunch analyses, the set of data points used for the background fit is fixed to the set identified by the nominal analysis. Not fixing the background definition would introduce a systematic bias in the per-run results, making the results across runs more difficult to compare. The t_0 parameter is optimized for each run and is expected to be randomly distributed, in the absence of any known changes to injection over time.

Fig. 14 shows C_E as a function of run number. These are the smallest subsets of data considered in this analysis, and the Fourier method tends to break down for runs with exceptionally low statistics. Consequently, a cut of 10^7 hits has been applied to the set of run numbers in order to ignore obvious outliers from poor method performance. The error bars are the statistical uncertainties, scaled from the nominal statistical uncertainty analysis by $\sqrt{N_{\text{dataset}}/N_{\text{run}}}$, where N is the number of hits.

Weighting each run by its statistics, the averaging of them all yields the results in Table 8, which are in good agreement with the results presented previously for all the calorimeters, bunches, and runs combined. This indicates that the per-calorimeter, per-bunch, and per-run information may be linearly combined before or after performing the fast rotation analysis.

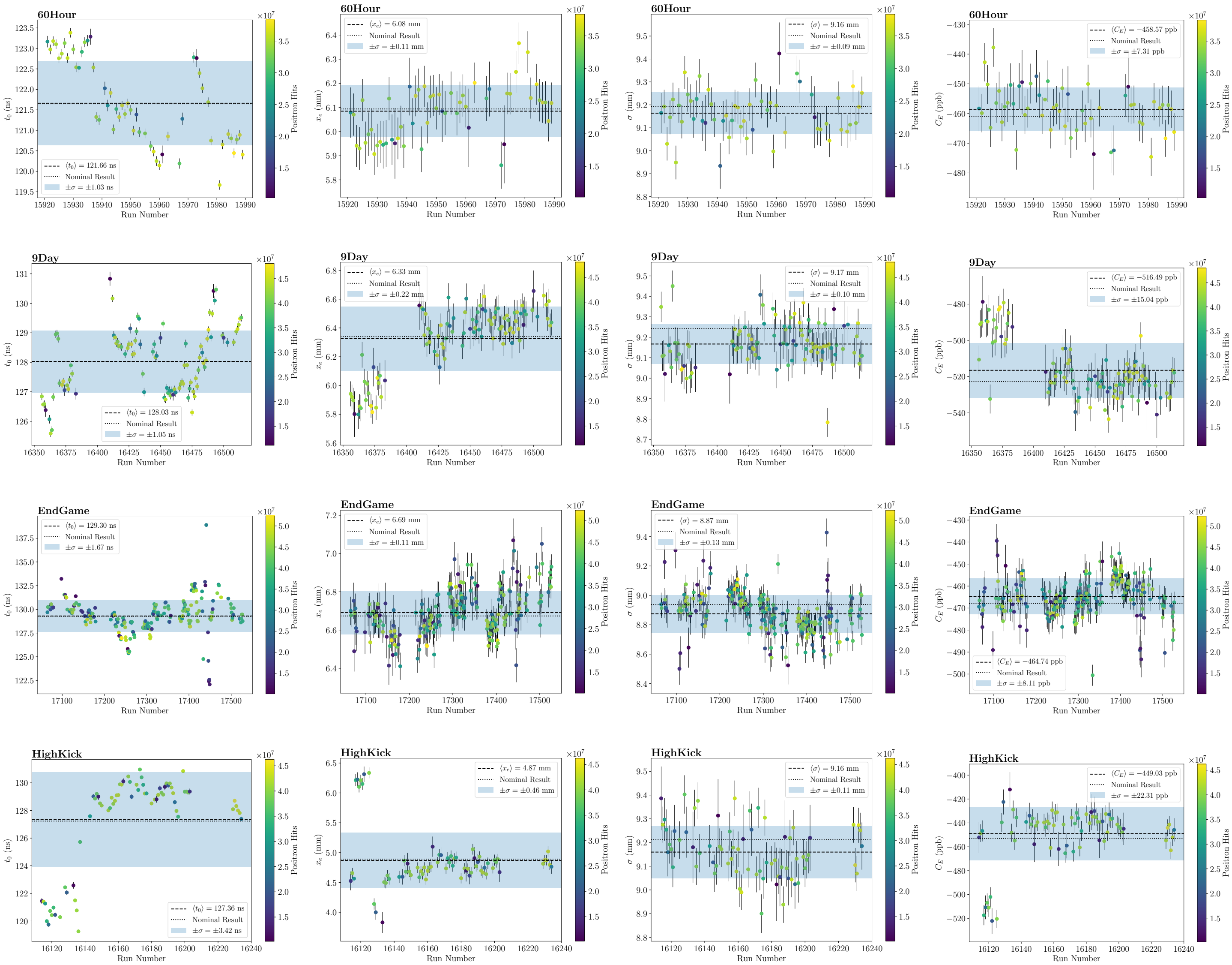

Figure 14: Per-run results from the fast rotation analysis. Error bars show statistical uncertainty (see Sec. 6).

6 Statistical uncertainty

6.1 Nominal analysis

This section will detail the estimation of the statistical uncertainty. The estimation relies on bootstrapping to generate many pseudo-datasets with varied statistics. Figure 15 shows a diagram of the procedure. Each pseudo-dataset is generated by varying the statistics of the original positron count histogram using all calorimeters, bunches, and runs combined. The number of entries N_i in each bin i is varied randomly by either $\pm\sqrt{N_i}$ (discretely), i.e. the variation follows Poisson statistics, given that the positron-count histogram corresponds to a counting experiment. The fast rotation analysis is performed on each of the many pseudo-datasets in order to get an ensemble of results, from which the statistical uncertainty is estimated as the one-sigma variation. The definition of the background, i.e. which data points are used in the background fit, is fixed when analyzing each of the pseudo-datasets. This is necessary to avoid a systematic effect due to the background definition[4]. The parameters t_0, t_s, and t_m are optimized for each pseudo-dataset.

Figure 16 shows the ensemble of results for each tracked variable in the nominal fast rotation analysis. The statistical uncertainty for a particular variable is taken as the standard deviation of its distribution; these uncertainties are tabulated in Table 9 The ensemble of pseudo-experiments is also generated using Bunch 0 alone and Calorimeter 1 alone, as representative samples of the per-bunch and per-calorimeter statistical uncertainties. Table 9 summarizes the numbers for each of the nominal, per-bunch, and per-calorimeter cases. The per-bunch and per-calorimeter results appear to scale from the nominal results by approximately $\sqrt{8}$ and $\sqrt{24}$, as expected from the corresponding reductions in statistics. Using this, we can extrapolate the appropriate statistical uncertainties for other subsets of the data which would be cumbersome to analyze individually using this method. In particular, the per-run analysis consists of hundreds of subsets with varying statistics, such that no single run can be chosen as a representative sample to analyze. Furthermore, the Fourier transform becomes increasingly unstable with the very low per-run statistics, so for systematic reasons an ensemble of per-run pseudo-experiments would be ill-suited for analysis. Consequently, statistical error bars throughout this document have been scaled from the nominal statistical uncertainties as $\sqrt{N_{\text{dataset}}/N_{\text{subset}}}$, with the per-bunch and per-calorimeter results taken as empirical verification. Overall, the statistical uncertainty is almost negligibly small compared to the systematic uncertainties (see Sec. 7).

Figure 17 shows the statistical correlation distributions between the results. It appears that x_e is very strongly anti-correlated with t_0. This is explained by the fact that changing t_0 skews the cosine Fourier transform to the right or the left, therefore shifting its average value one way or the other.

[4]This effect would translate into multiple peaks in the distribution of the results. These peaks would have the same standard deviation but different average values.

Dataset	Analysis	σ_{t_0} (ns)	σ_{x_e} (mm)	σ_σ (mm)	σ_{C_E} (ppb)
60Hour	nominal	0.016	0.012	0.010	0.90
	per-bunch	0.043	0.032	0.028	2.46
	per-calorimeter	0.078	0.057	0.047	4.17
9Day	nominal	0.013	0.009	0.008	0.82
	per-bunch	0.033	0.024	0.019	1.99
	per-calorimeter	0.062	0.045	0.035	3.74
EndGame	nominal	0.006	0.005	0.005	0.34
	per-bunch	0.019	0.015	0.015	1.05
	per-calorimeter	0.028	0.021	0.023	1.56
HighKick	nominal	0.015	0.011	0.010	0.96
	per-bunch	0.041	0.030	0.027	2.58
	per-calorimeter	0.075	0.055	0.045	4.54

Table 9: Statistical uncertainties of the nominal, per-bunch, and per-calorimeter fast rotation analyses. Notice that the per-bunch and per-calorimeter results scale from the nominal results by approximately $\sqrt{8} \approx 2.8$ and $\sqrt{24} \approx 4.9$, as expected from the relative factors of $1/8$ and $1/24$ in statistics.

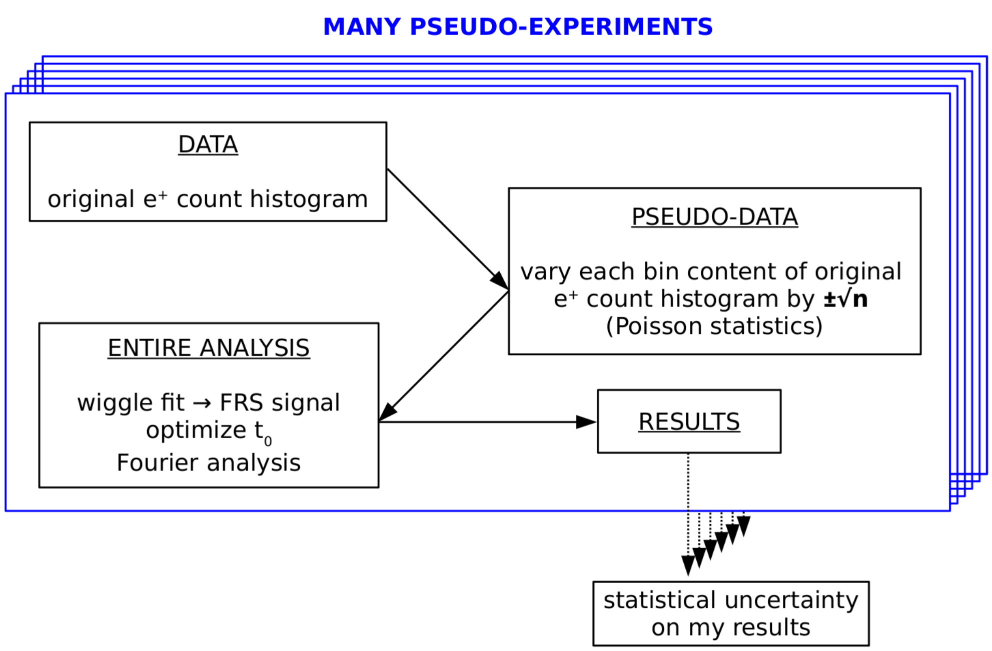

Figure 15: Diagram of the procedure for estimating the statistical uncertainty on the fast rotation results.

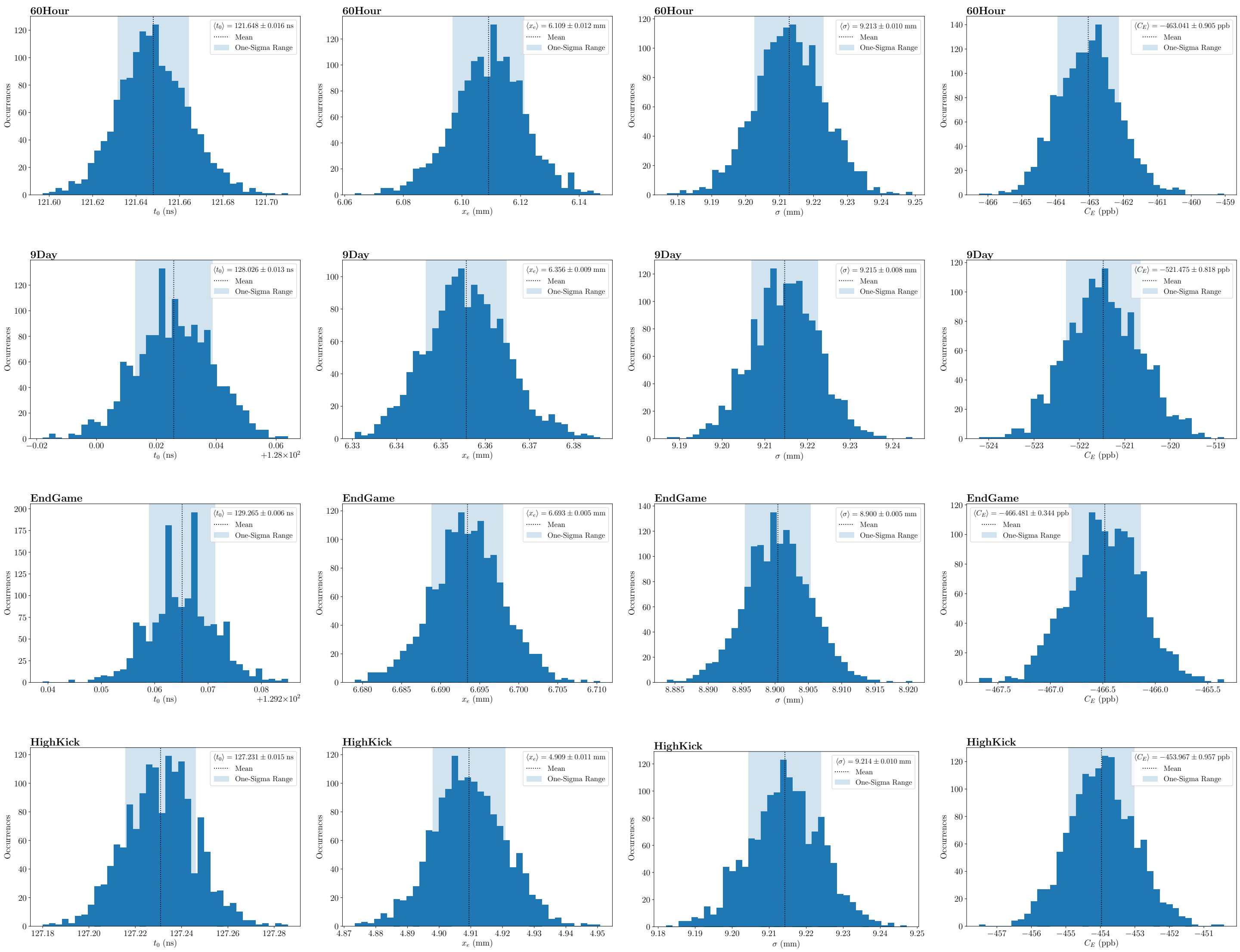

Figure 16: Analysis results from the statistically varied pseudo-data in the nominal case (all calorimeters, bunches, and runs combined). Approximately 1500 pseudo-experiments were performed for each dataset. The rows are in the order of t_0, x_e, σ, and C_E, with datasets along the columns.

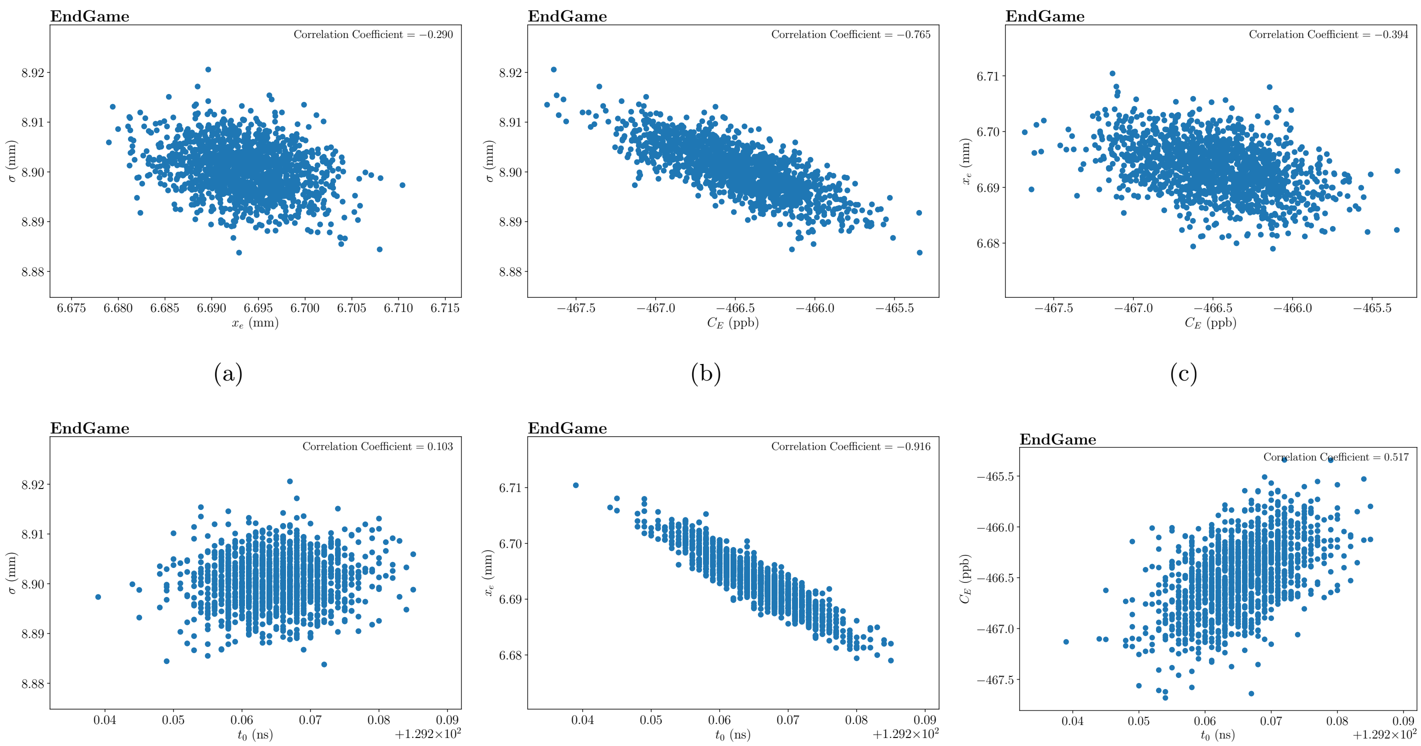

(a) (b) (c)

(d) (e) (f)

Figure 17: Statistical correlations between each pair of tracked variables in the Run-1 EndGame dataset: (a) x_e and σ, (b) C_E and σ, (c) C_E and x_e, (d) t_0 and σ, (e) t_0 and x_e, and (f) t_0 and C_E.

7 Systematic uncertainties

The primary philosophy of the systematic uncertainty estimation is to vary the analysis parameters and observe the corresponding change in results. We then estimate the systematic uncertainty associated with a given parameter as the standard deviation of the spread in the results.

7.1 t_0 systematic

As shown in Sec. 4.1 of [2], sub-nanosecond knowledge of the t_0 parameter is essential in order to reach the target $\mathcal{O}(10)$ ppb uncertainty on C_E. For example, Figure **??** shows how x_e, σ, and C_E vary as a function of t_0 over a one-nanosecond range. We see that the small change in σ drives a wide variation of 50 ppb in C_E, whereas the relatively larger change in x_e does not significantly impact C_E. This is because x_e and σ both contribute to C_E as squares ($C_E \propto \sigma^2 + x_e^2$), and typically $\sigma > x_e$, so in that case σ^2 weighs much more heavily in C_E.

In order to estimate the uncertainty in the optimized t_0, as detailed in Sec. 4.1 of [2], we perform the optimization and analysis procedure using three different fit functions for the background, which we call the cardinal sine function, the error function, and the triangle-based function. (These originate from the choice of an ansatz frequency distribution which is used to fill in the missing time between t_0 and t_s: a delta function yields the cardinal sine correction, a Gaussian yields the error function correction, and an asymmetric triangle yields the "triangle-based" correction.) Table **??** shows the uncertainty results, estimated as the RMS of the results from the three background fit functions.

7.2 t_s systematic

In an ideal world—that is, if usable data were available from injection—the fast rotation Fourier analysis should be performed from a start time of $t_s = t_0$ onward, since the cosine transform performs an even extension about t_0 (see Sec. 4.1). However, given the positron contamination during the injection flash, the earliest the fast rotation analysis can begin is about $t_s \sim 4$ μs. Furthermore, scraping shifts the closed orbit of the beam until about 25 μs, with the first-to-second-step transition happening at about 7 μs. To avoid these systematic effects, the ω_a analysis begins nominally at around 30 μs, when the beam has stabilized after the scraping period. Because C_E is a correction to ω_a, we should try to match the measurement of C_E to the same muon population used to measure ω_a. Otherwise, using data before 25 μs could bias the reconstructed radial distribution, such that the resulting C_E is not truly representative of the muon population which survives past 30 μs. Therefore, it desirable to delay the fast rotation analysis start time further to $t_s \sim 30$ μs. There are also other systematic effects which contribute more strongly at early times, such as the instantaneous pileup rate, the gain correction, and muon losses. It is thus essential to show that the fast rotation results change within an acceptable range between the earliest possible $t_s \sim 4$ μs and the optimal $t_s \sim 30$ μs.

The t_s scan (see [2] Sec. 4.2) is performed using the triangle-based background fit function. The t_0 value is fixed to the optimized result from the nominal analysis (where $t_s = 4$ μs), given that the t_0 optimization procedure performs best for the earliest start times. The definition of the background is also fixed to the one found in the nominal analysis. Figure 19 shows the results of the analysis as a function of t_s between 4 and 30 μs. The statistical uncertainty on each point is not shown, but increases exponentially with time since the fast rotation statistics decreases exponentially (due to the muon lifetime). For context, Figure 18 shows a range of background fits using the triangle-based function for six different t_s values, from the EndGame dataset.

The trend of the results cannot currently be explain with satisfaction. Tentative explanations could be made using arguments related to beam dynamics and scraping. For instance, the first step of scraping moves the radial closed orbit at early times and scrapes the radial tail of the beam, thus shifting the equilibrium radius and shrinking the width of the beam. The second step then re-centers the beam, allowing its width to grow and its equilibrium radius to move. These tentative arguments need to be thoroughly investigated with full-scale high-statistics simulations using `BMAD` and `GM2RINGSIM`. For now, we estimate the systematic uncertainty due to t_s as the RMS of the results between 4 and 25 μs, which is the range of start times where the background subtraction procedure (using the triangle-based fit function) has been shown to be effective in toy Monte Carlo studies [2]. Beyond this time, the background subtraction procedure typically fails to perform well, and hence the results are not usable for the purposes of this scan. The systematic uncertainty estimates are tabulated in Table **??**.

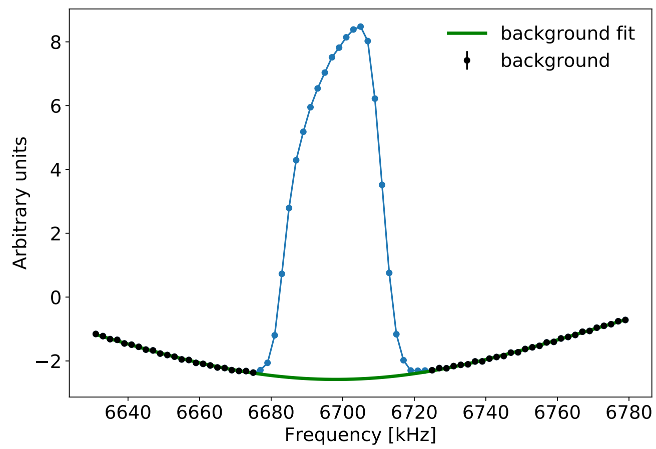

(a)

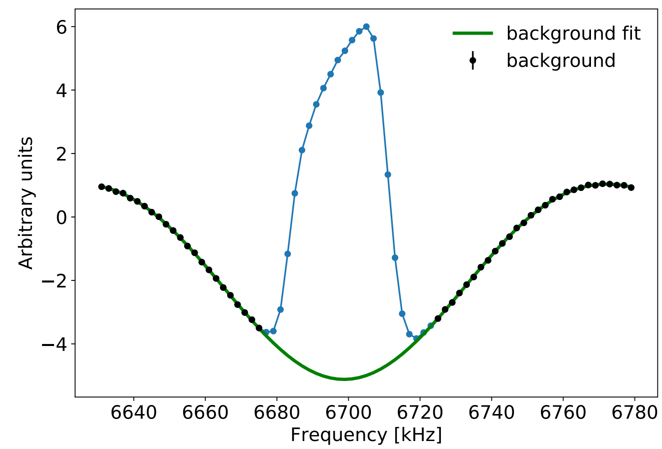

(b)

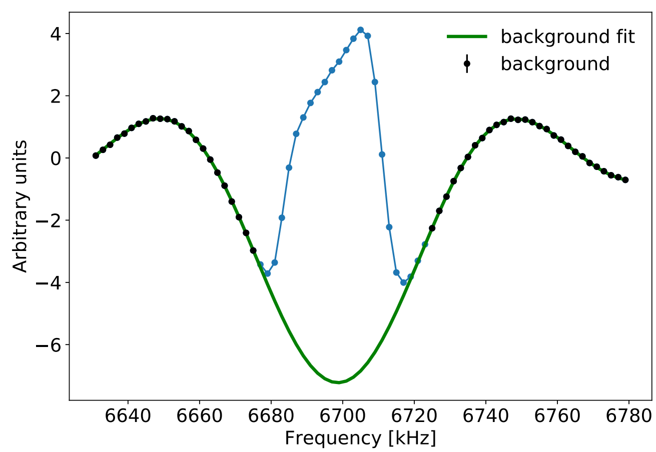

(c)

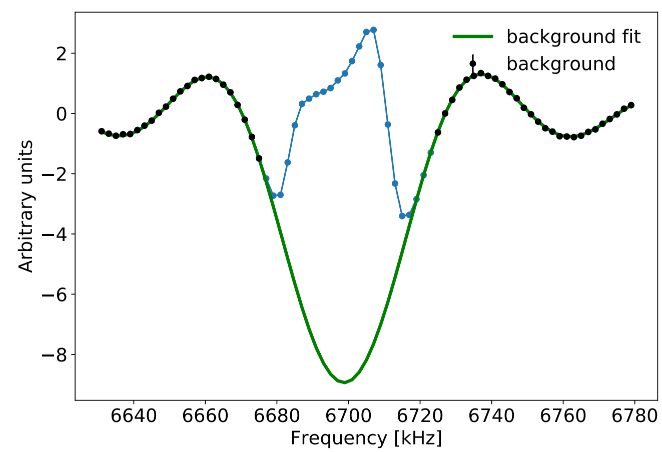

(d)

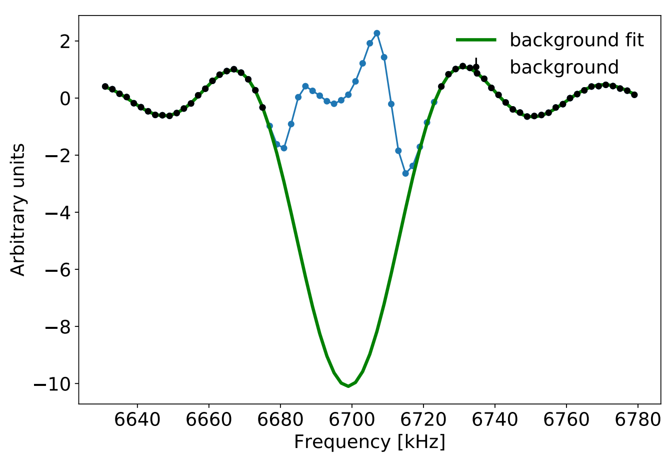

(e)

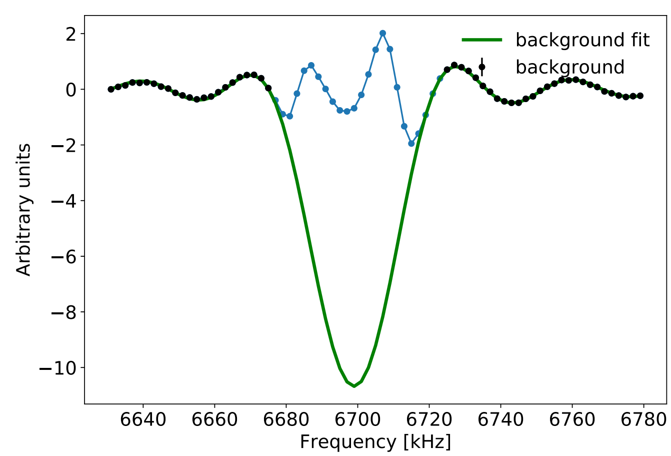

(f)

Figure 18: Background fit of the cosine Fourier transform using the triangle-based function in the EndGame dataset: (a) $t_s = 5\ \mu s$, (b) $t_s = 10\ \mu s$, (c) $t_s = 15\ \mu s$, (d) $t_s = 20\ \mu s$, (e) $t_s = 25\ \mu s$, (f) $t_s = 30\ \mu s$.

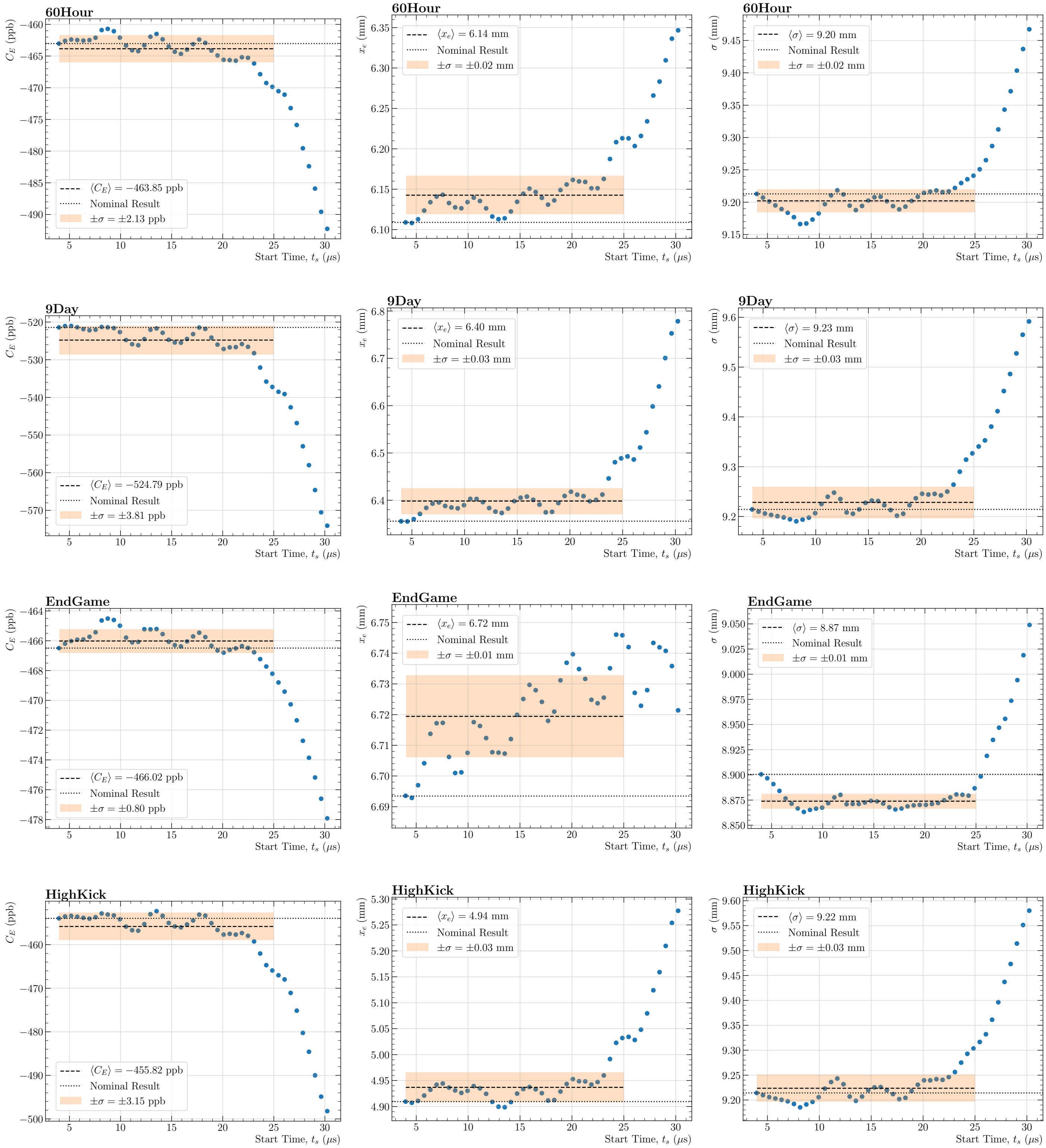

Figure 19: Results of the fast rotation analysis as a function of t_s for a 30 μs range, using the triangle-based background fit function. The shaded regions denote the RMS spread used to estimate the systematic uncertainty.

7.3 t_m systematic

As explained in [1], Sec. 7.3, and [2], Sec. 4.2, when increasing the length of the fast rotation signal there is a trade-off between improving statistics and worsening noise. To optimize this trade-off, we perform a scan over the end time t_m for the cosine transform of the fast rotation signal. Figure 21 shows the fast rotation analysis results as a function of t_m for $t_s = 4$ μs. For each t_m value, the analysis is performed with its nominal configuration. Overall, the results appear the most stable for t_m values between 150-300 μs. Before 150 μs, low statistics yields poor resolution in the frequency distribution. After 300 μs, increasing statistical noise in the fast rotation signal (see Fig. 3(f)) distorts the frequency distribution. For context, Figure 20 shows the background fit to the cosine Fourier transform for six values of t_m (using the sinc fit function) from the EndGame dataset. The systematic uncertainty is taken as the RMS of the results between 150 and 300 μs. The variation in the results could be due to spectral leakage, given the small size of the statistical uncertainty and the very high statistical correlation between consecutive data points in the scan.

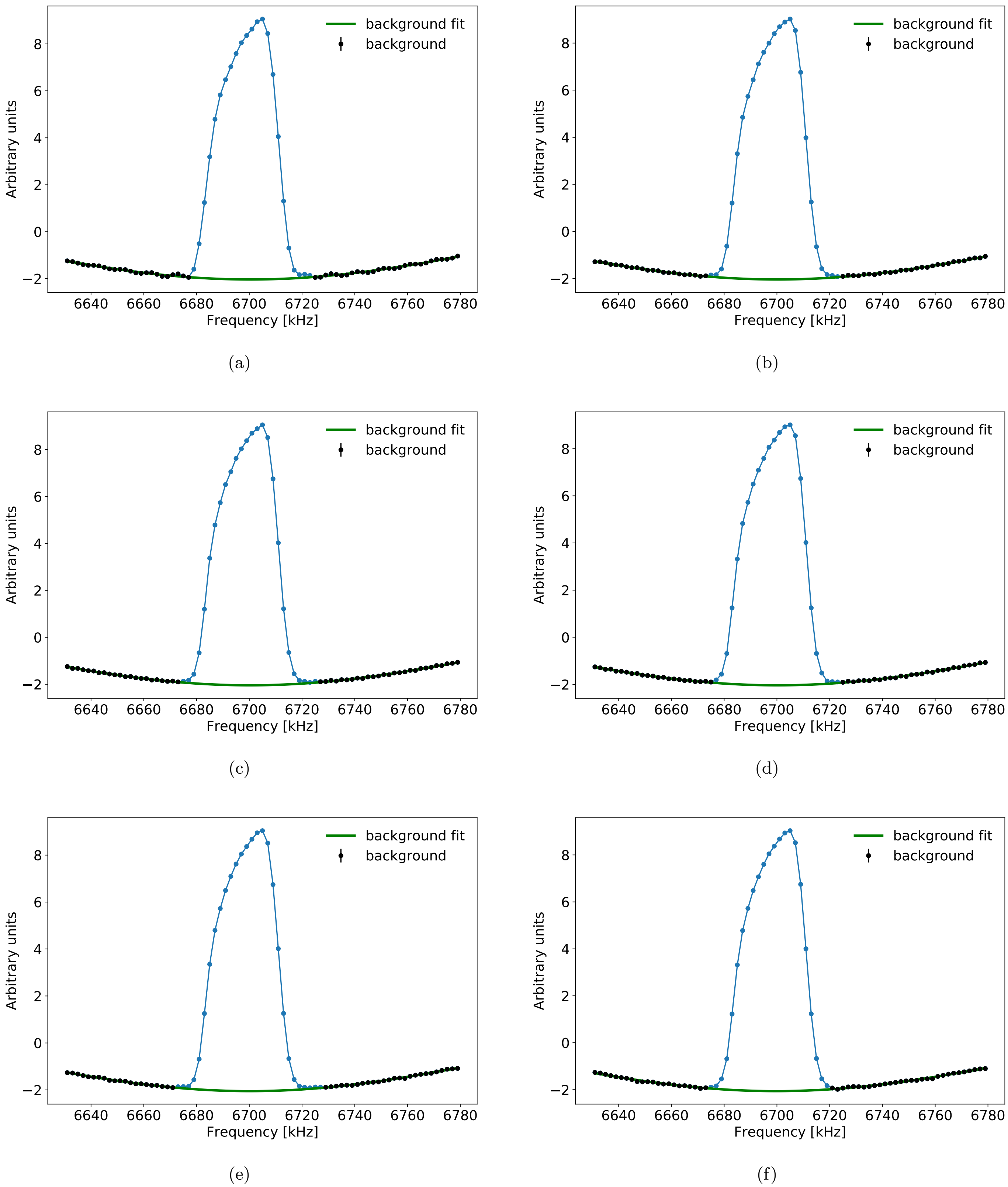

Figure 20: Background fit to the cosine Fourier transform for different t_m values: (a) 100, (b) 150, (c) 200, (d) 300, (e) 400, and (f) 500 μs.

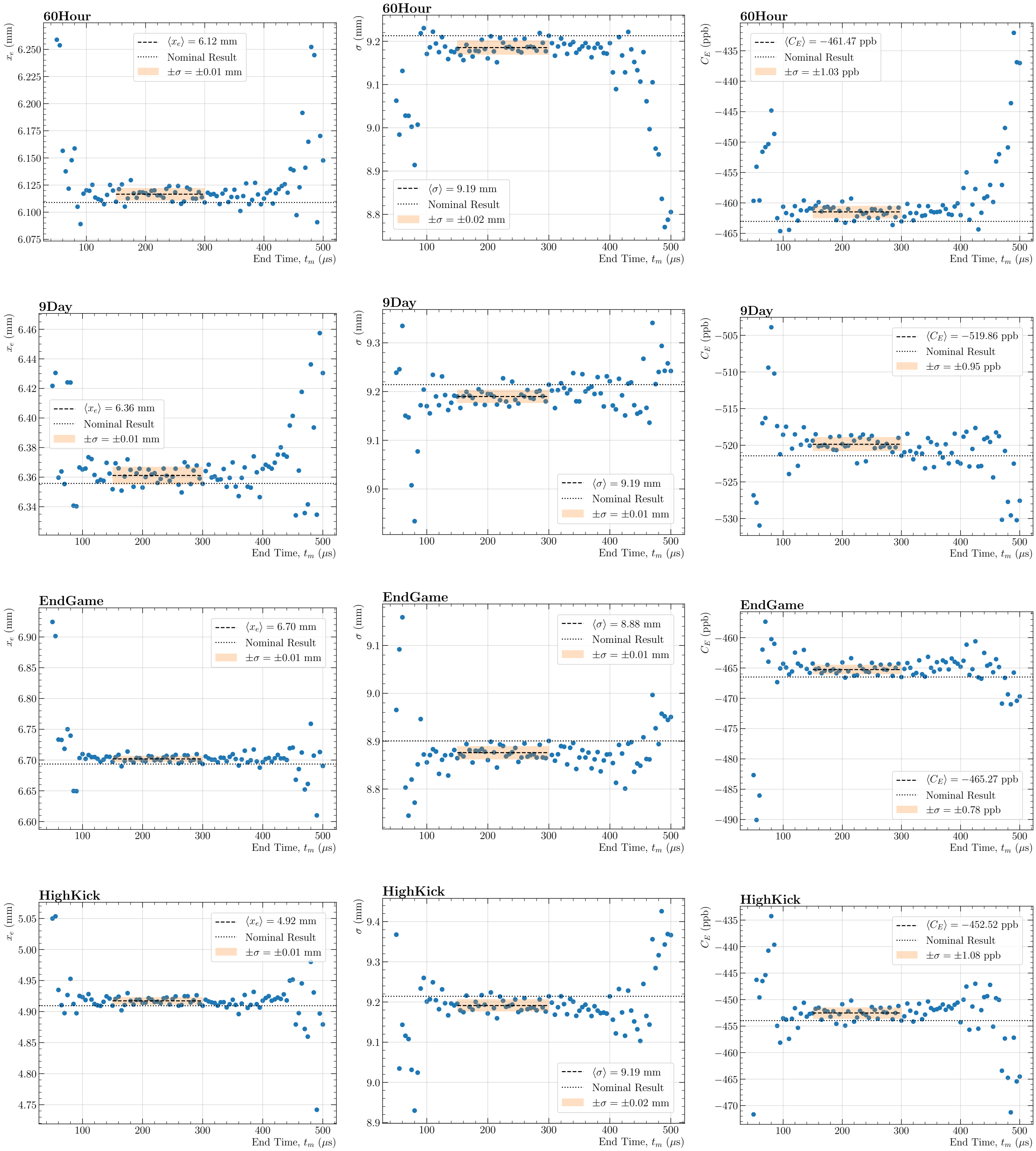

Figure 21: Results of the fast rotation analysis as a function of t_m, for $t_s = 4\ \mu s$. The shaded regions denote the RMS spread used to estimate the systematic uncertainty.

7.4 Frequency interval

As explained in [1], Sec. 7.3, and [2], Sec. 4.4, the nominal frequency interval used to produce the cosine Fourier transform is 2 kHz. This is smaller than the intrinsic frequency resolution set by the number of bins and time interval of the fast rotation signal. For $t_s = 4\ \mu$s and $t_m = 300\ \mu$s, with a 1-ns time interval, the intrinsic frequency resolution is

$$\frac{1}{\text{time interval} \times \text{number of bins}} = \frac{1}{10^{-9}\ \text{s} \times 296000} = 3.34\ \text{kHz}.$$

Using a frequency interval of 2 kHz leads to over-sampling, responsible for the modulation seen in Fig. 20(a) for instance. Over-sampling was shown in toy Monte Carlo studies to be sound (see [2], Sec. 4.4). Nonetheless, a frequency interval scan is performed to ensure the same behavior in the data. Figure 23 shows the fast rotation results as a function of frequency interval. The allowed values for the frequency interval are chosen such that an integer number of bins fit within the full frequency range used for the cosine Fourier transform. The results appear stable for a frequency interval up to 2.5 kHz. This behavior is the same as the one observed in toy Monte Carlo studies (see [2], Sec. 4.4). The systematic uncertainty is taken as the RMS of the results between 0.25 kHz and 3.75 kHz.

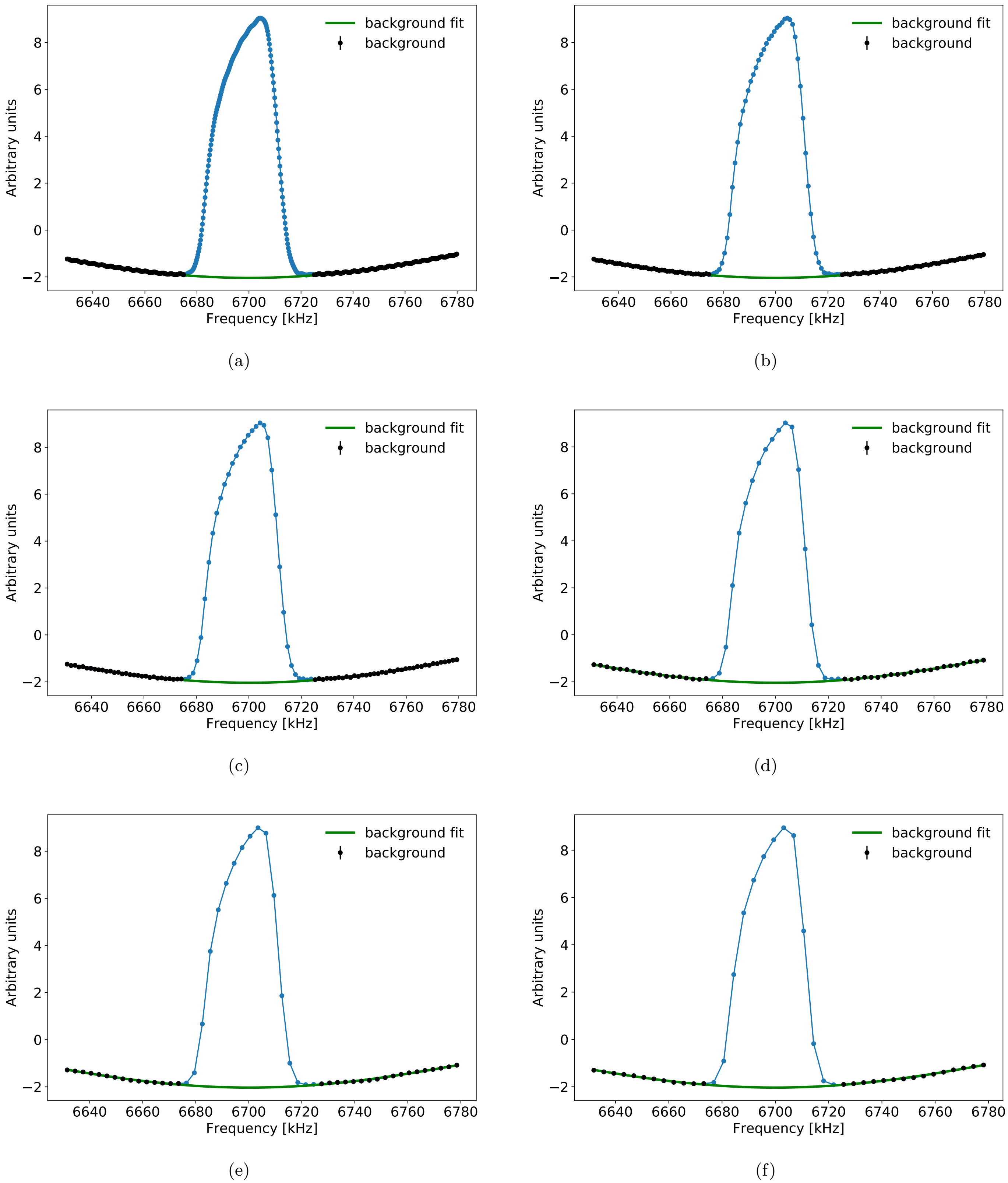

Figure 22: Background fit to the cosine Fourier transform from the EndGame dataset for different frequency intervals: (a) 0.25, (b) 1.0, (c) 1.5, (d) 2.5, (e) 3.0, and (f) 3.75 kHz.

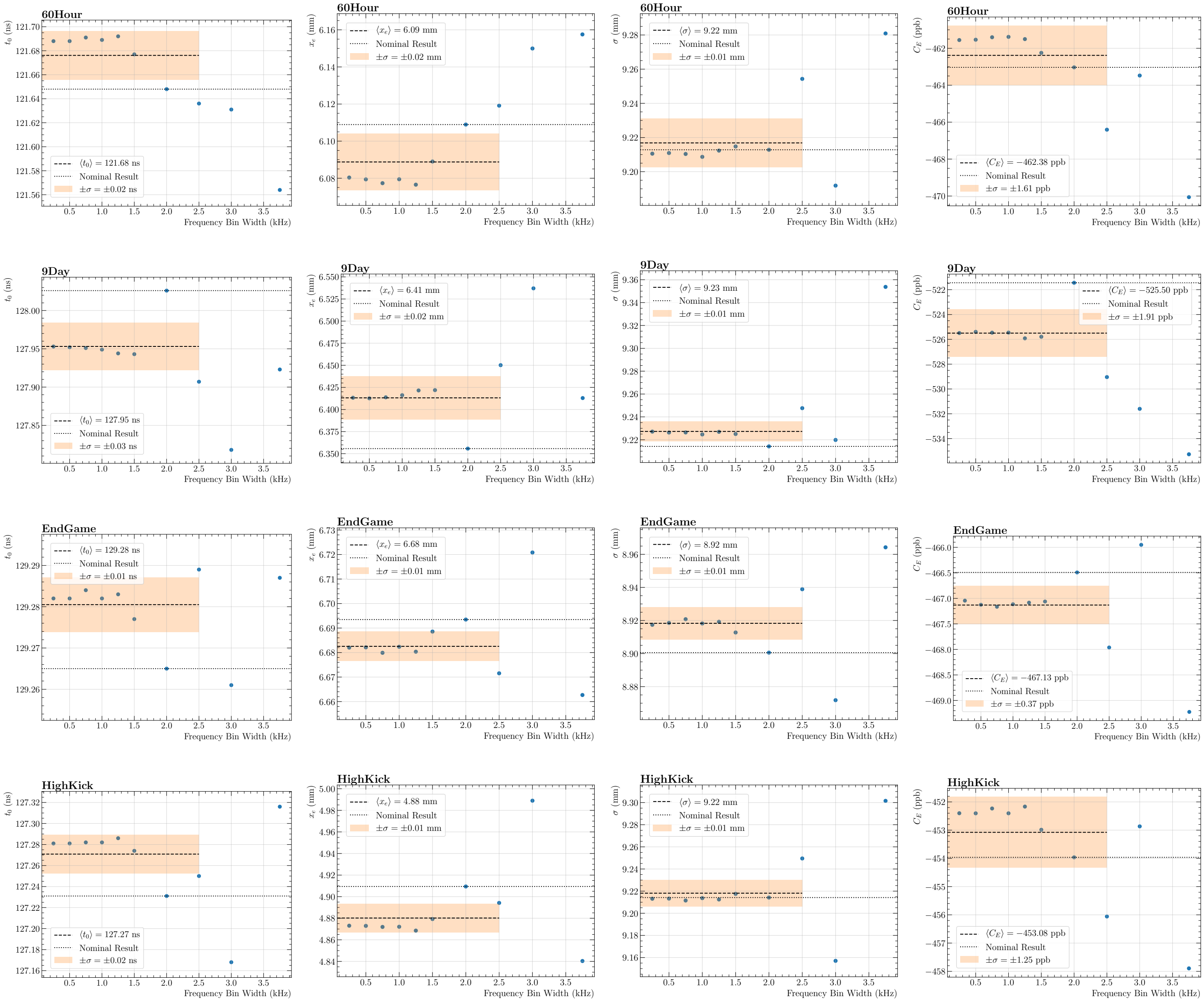

Figure 23: Results of the fast rotation analysis as a function of the frequency interval. The shaded regions denote the RMS spread used to estimate the systematic uncertainty.

7.5 Background

The definition of the background is key for optimizing t_0 and correcting the cosine Fourier transform. The functional form of the background is already part of the t_0 systematic uncertainty. Other sources of uncertainty from the background have to do with how it is defined, and how statistical fluctuations can affect the analysis results.

7.5.1 Background definition

The background of the cosine Fourier transform is defined as the set of data points within $\pm N\sigma_{\mathrm{bkgd}}$ of the fit, where σ_{bkgd} is the statistical noise of the background, estimated from the fit residuals for the optimal t_0 value. By varying the parameter N, nominally taken as $N = 2$, the set of points accepted into the background definition will change. In particular, the residuals are larger near the edges of the central peak, so larger N values cause the background fit to extend farther inward; smaller N values keep the background fit farther away from the central peak. Figure 24 shows the background fit from the EndGame dataset for $N = 1$ and $N = 5$, demonstrating this effect. Figure 25 shows the results of a scan over the background definition threshold N. Similar to what we observe in toy Monte Carlo studies (see [2], Sec. 4.5), the width of the radial distribution decreases as N increases. This is because the background definition includes more inner samples near the central peak, which pulls the center of the background fit slightly upward, reducing the size of the correction to the edges of the distribution, thereby reducing the width in consequence. The systematic uncertainty is taken as the RMS of the results across the scan.

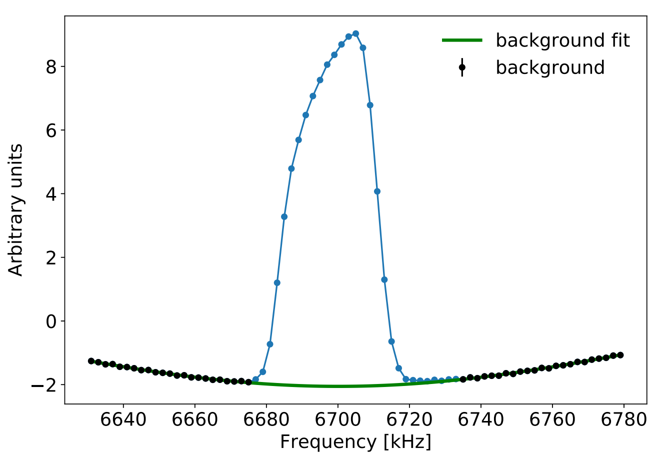

(a)

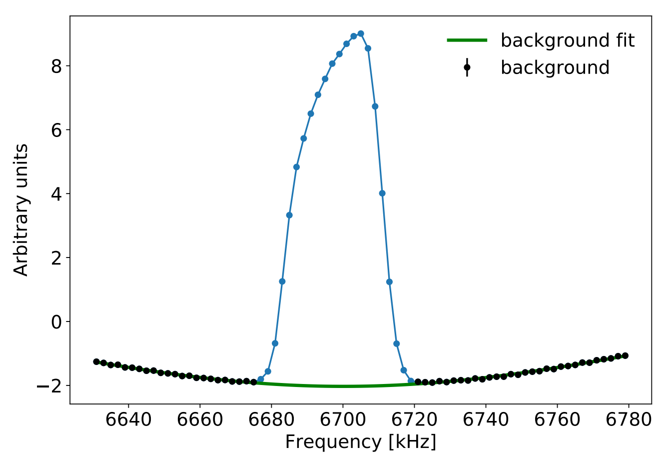

(b)

Figure 24: Background fit to the cosine Fourier transform from the EndGame dataset for two background definition thresholds: (a) $N = 1$, and (b) $N = 5$.

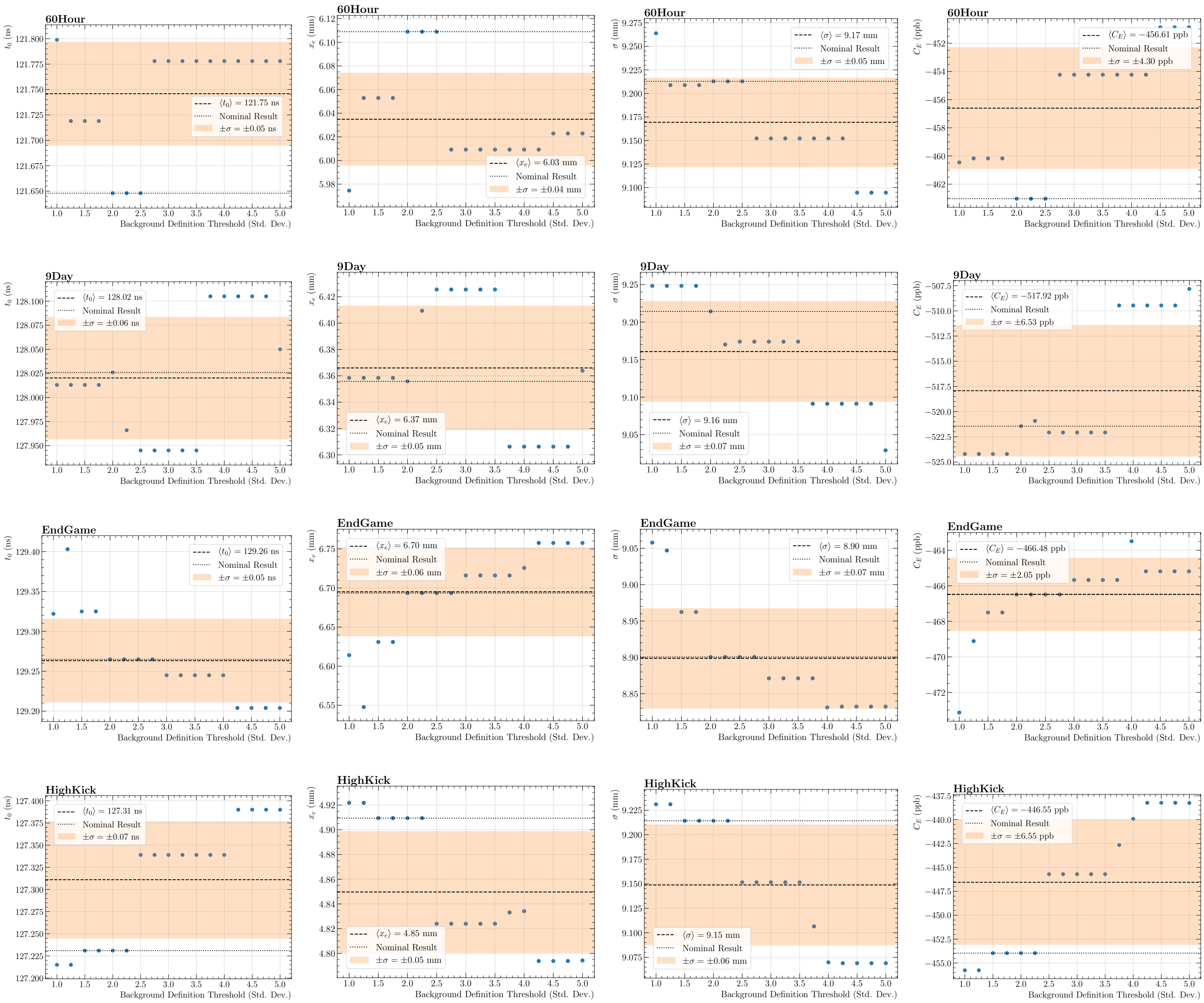

Figure 25: Results of the fast rotation analysis as a function of the background definition threshold N. The shaded regions denote the RMS spread used to estimate the systematic uncertainty.

7.5.2 Background removal

Statistical fluctuations in the tails (i.e. background regions) of the radial distribution can bias the extraction of the equilibrium radius and width. This effect is estimated by removing (i.e. zeroing out) the background regions of the radial distribution, where the data points within $\pm N \cdot \sigma_{\mathrm{bkgd}}$ of the background fit function are zeroed out. This background removal threshold N plays a very similar role as N in the previous section on the background definition, but is varied independently. Figure 26 shows the results of the background removal scan. The systematic uncertainty is taken as the RMS of the results across the scan.

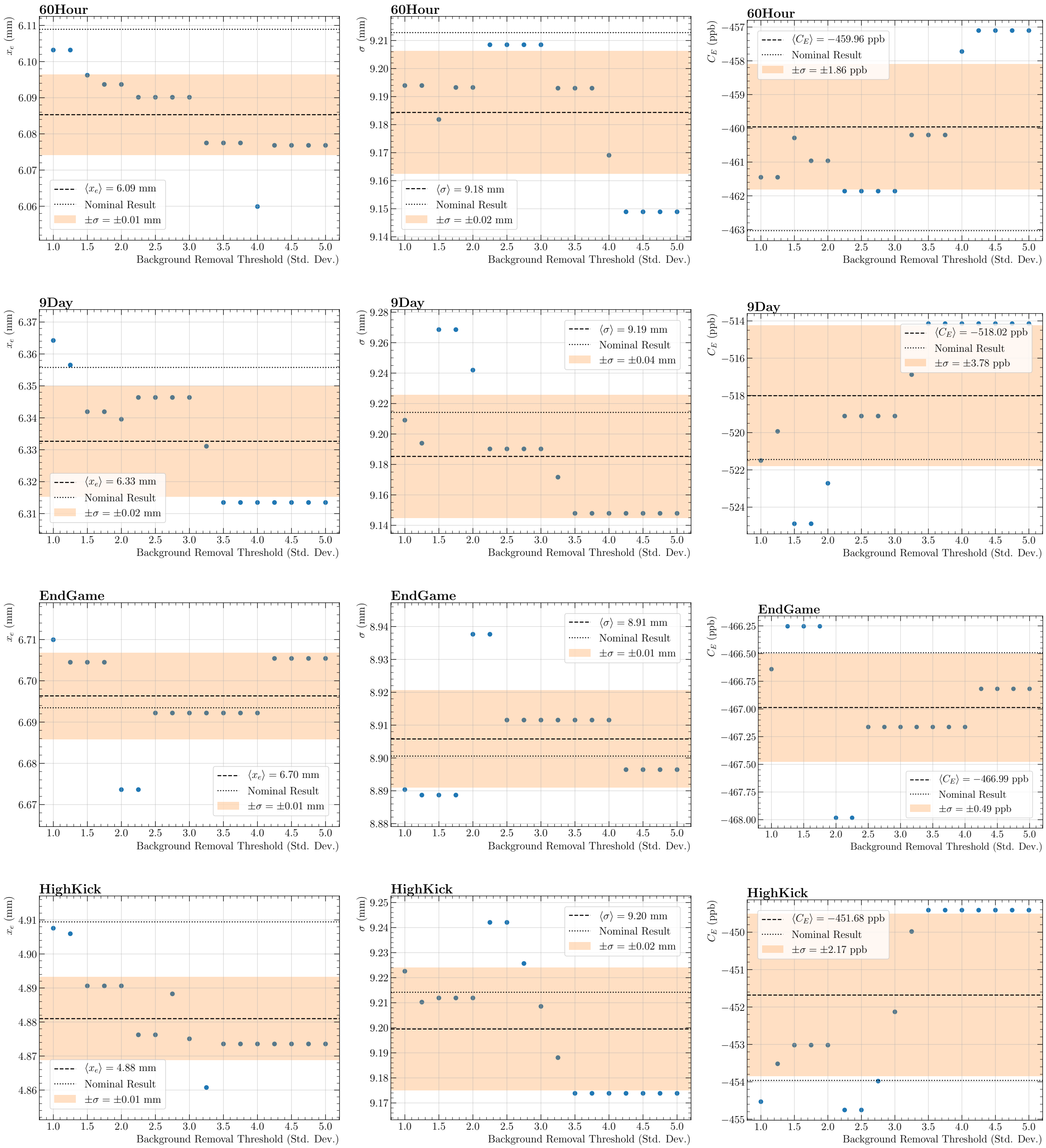

Figure 26: Results of the fast rotation analysis as a function of the background removal threshold N. The shaded regions denote the RMS spread used to estimate the systematic uncertainty.

7.6 Wiggle fit

The nominal fit to the positron-count histogram is the 9-parameter fit, incorporating the muon lifetime, anomalous spin precession, and CBO modulation. The anomalous spin precession frequency analysis uses a fit to the positron-count histogram with many more parameters, including the effects of pileup, the vertical waist modulation, muon losses, etc. In order to estimate the importance of the accuracy of the fit to the data, the analysis is performed on fast rotation signals produced using a different number of parameters in the wiggle fit: 2 (muon lifetime only), 5 (muon lifetime and anomalous spin precession), and 9 (muon lifetime, anomalous spin precession, and CBO modulation). The results are consistent within the statistical uncertainties of x_e, σ, and C_E. This is not surprising, because the anomalous spin precession and CBO frequencies (and aliases thereof) do not overlap with the frequency range of the cyclotron motion. However, the exponential decay from the muon lifetime does interfere with the cyclotron region of the frequency domain, and hence must be removed from the positron-count histogram.

Since pileup, muon losses, etc. are not included in the fit functions, the question of their impact on the fast rotation analysis remains. The t_s scan provides a good handle on these effects, because their relative impact decreases significantly over the first 30 μs of the fill, and therefore are part of the systematic uncertainty associated with the t_s scan.

7.7 Positron energy threshold

The nominal positron energy threshold used to produce the positron-count histograms for all of the above studies was 1500 MeV. However, the anomalous spin precession frequency analysis is performed for a variety of energy thresholds and energy weighting schemes. Therefore, it is important to perform the fast rotation analysis as a function of positron energy. Here we perform the fast rotation analysis (with fixed background definition) on fast rotation signals produced using a range of positron energy bins and thresholds. Figure 28 shows the results of the fast rotation analysis as a function of positron energy threshold, and Figure 27 shows the results over self-contained positron energy bins. In both cases, there is a clear upward trend in x_e and σ with increasing positron energy. This effect is believed to be related to calorimeter acceptance rather than beam dynamics.

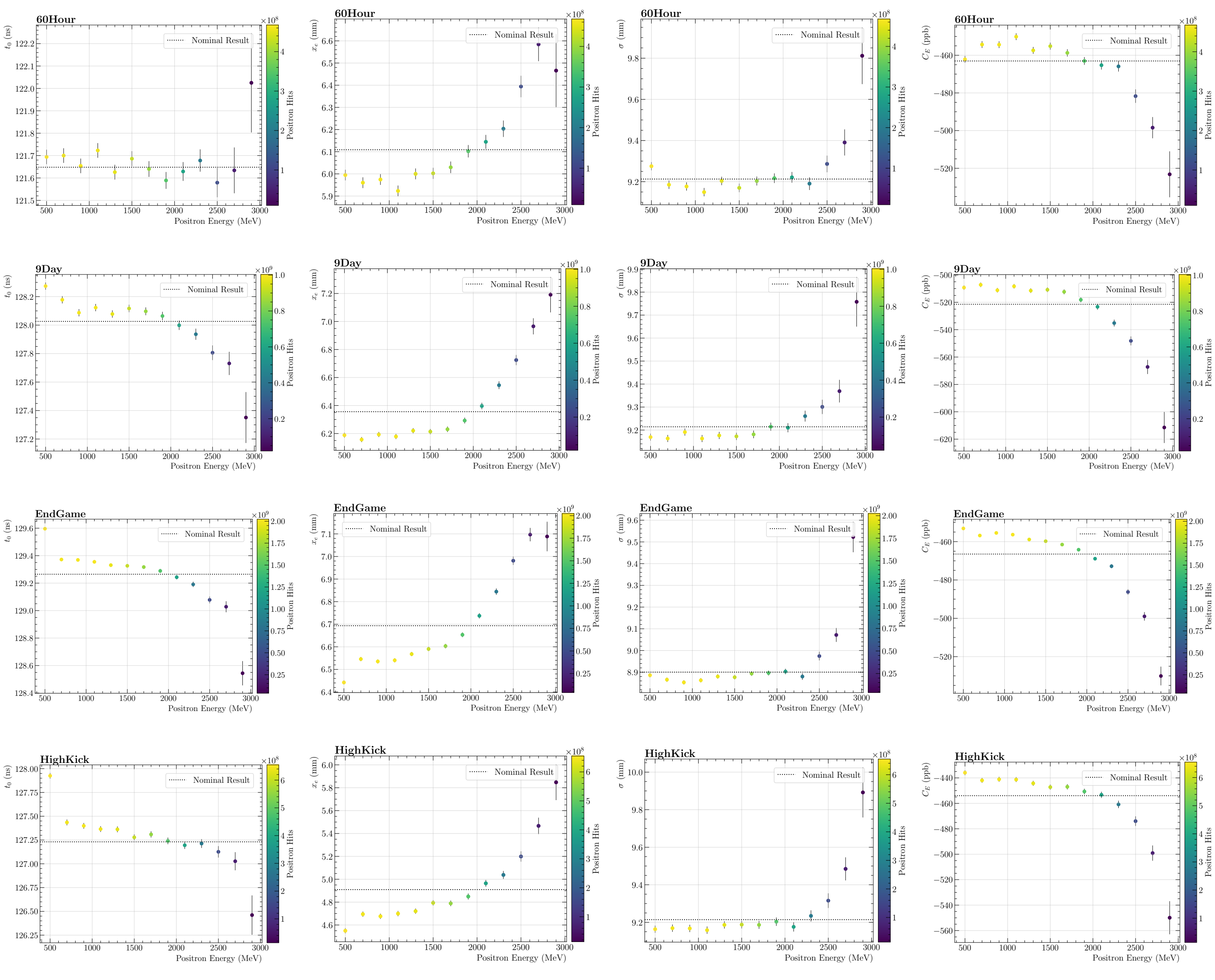

Figure 27: Results of the fast rotation analysis as a function of positron energy. The data points shown are the left edges of the energy bins in steps of 200 MeV.

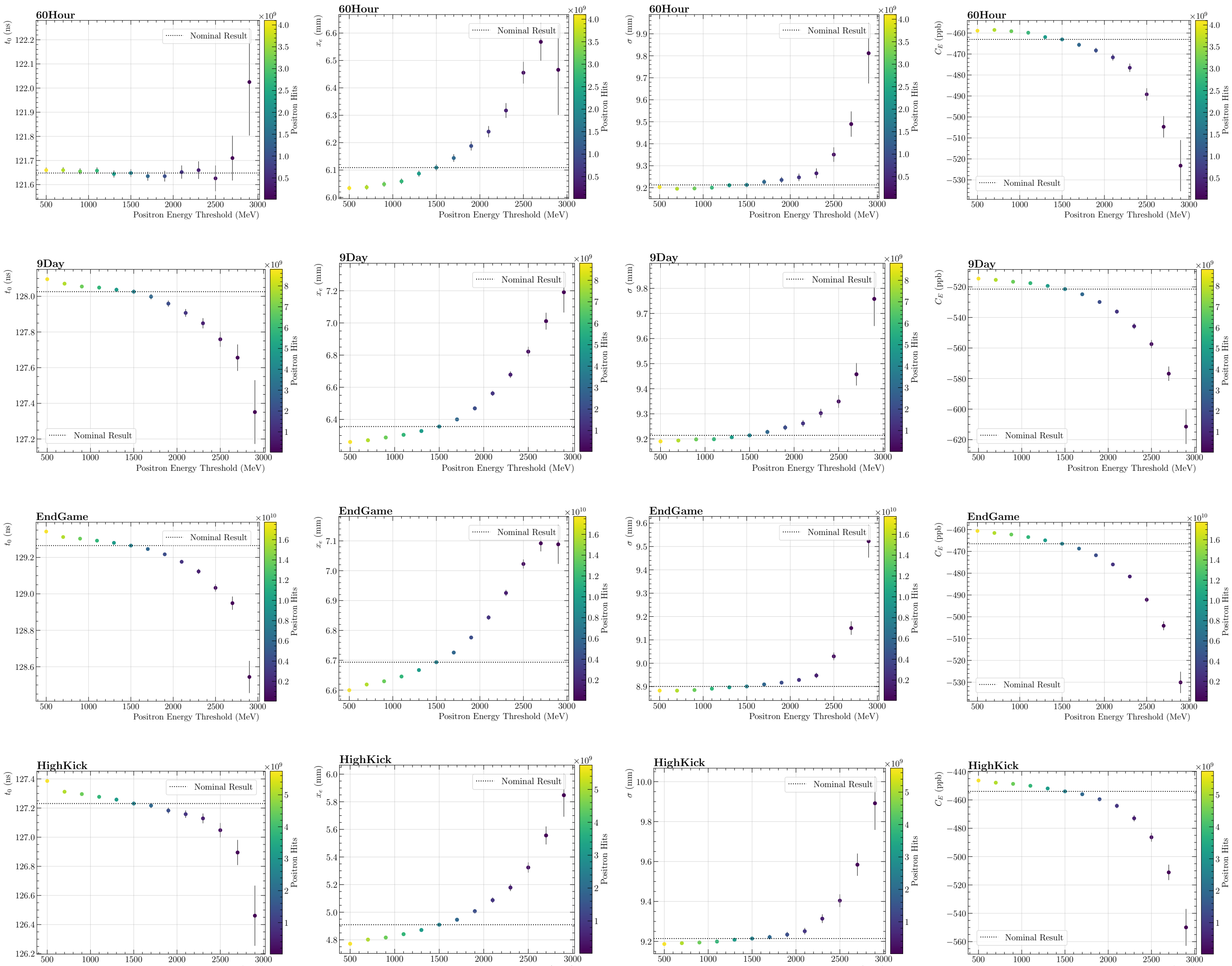

Figure 28: Results of the fast rotation analysis as a function of positron energy threshold, including energies from the data points shown up to the maximum of 3.1 GeV.

60Hour

lower energy	bin result	threshold result	avg. bin result
500	462.2 ± 1.8	458.9 ± 0.6	459.1 ± 0.6
700	454.3 ± 1.8	458.5 ± 0.6	458.7 ± 0.6
900	454.4 ± 1.8	459.1 ± 0.7	459.3 ± 0.7
1100	450.1 ± 1.8	459.8 ± 0.7	460.1 ± 0.7
1300	457.4 ± 1.8	461.9 ± 0.8	462.1 ± 0.8
1500	455.2 ± 1.9	463.0 ± 0.9	463.3 ± 0.9
1700	458.7 ± 1.9	465.6 ± 1.0	465.8 ± 1.0
1900	463.0 ± 2.1	468.3 ± 1.2	468.7 ± 1.2
2100	465.3 ± 2.3	471.6 ± 1.5	471.7 ± 1.5
2300	465.9 ± 2.7	476.5 ± 2.0	476.5 ± 2.0
2500	481.7 ± 3.6	489.2 ± 2.9	488.7 ± 2.9
2700	498.4 ± 5.6	504.7 ± 5.1	502.8 ± 5.1
2900	523.2 ± 12.2	523.2 ± 12.2	523.2 ± 12.2

9Day

lower energy	bin result	threshold result	avg. bin result
500	509.3 ± 1.6	514.6 ± 0.5	514.7 ± 0.5
700	507.2 ± 1.6	515.4 ± 0.6	515.4 ± 0.6
900	511.2 ± 1.6	516.6 ± 0.6	516.6 ± 0.6
1100	508.3 ± 1.6	517.6 ± 0.7	517.5 ± 0.7
1300	511.5 ± 1.6	519.4 ± 0.7	519.4 ± 0.7
1500	510.8 ± 1.7	521.4 ± 0.8	521.3 ± 0.8
1700	512.3 ± 1.7	524.8 ± 0.9	524.6 ± 0.9
1900	518.2 ± 1.9	529.9 ± 1.1	529.6 ± 1.1
2100	523.3 ± 2.1	536.2 ± 1.4	535.7 ± 1.4
2300	535.2 ± 2.5	545.7 ± 1.8	545.2 ± 1.8
2500	548.2 ± 3.3	557.4 ± 2.7	556.9 ± 2.7
2700	567.2 ± 5.2	576.8 ± 4.7	574.9 ± 4.7
2900	611.5 ± 11.4	611.5 ± 11.4	611.5 ± 11.4

EndGame

lower energy	bin result	threshold result	avg. bin result
500	453.1 ± 0.7	460.6 ± 0.2	460.7 ± 0.2
700	456.8 ± 0.7	461.1 ± 0.2	461.7 ± 0.2
900	455.5 ± 0.7	462.3 ± 0.3	462.4 ± 0.3
1100	456.4 ± 0.7	463.4 ± 0.3	463.6 ± 0.3
1300	458.9 ± 0.7	464.9 ± 0.3	465.1 ± 0.3
1500	459.8 ± 0.7	466.5 ± 0.3	466.7 ± 0.3
1700	461.5 ± 0.7	468.7 ± 0.4	468.9 ± 0.4
1900	464.2 ± 0.8	471.8 ± 0.5	471.9 ± 0.5
2100	468.9 ± 0.9	476.0 ± 0.6	476.1 ± 0.6
2300	472.8 ± 1.1	481.5 ± 0.8	481.6 ± 0.8
2500	486.3 ± 1.4	492.2 ± 1.1	492.0 ± 1.1
2700	499.0 ± 2.2	504.1 ± 2.0	504.3 ± 2.0
2900	530.1 ± 4.9	530.1 ± 4.9	530.1 ± 4.9

HighKick

lower energy	bin result	threshold result	avg. bin result
500	435.9 ± 1.9	446.3 ± 0.6	446.6 ± 0.6
700	441.9 ± 1.9	447.8 ± 0.7	447.9 ± 0.7
900	441.1 ± 1.9	448.7 ± 0.7	448.8 ± 0.7
1100	441.3 ± 1.9	450.0 ± 0.8	450.1 ± 0.8
1300	444.3 ± 1.9	451.9 ± 0.9	451.9 ± 0.9
1500	447.3 ± 2.0	454.0 ± 1.0	453.8 ± 1.0
1700	447.0 ± 2.1	456.0 ± 1.1	455.8 ± 1.1
1900	450.7 ± 2.2	459.5 ± 1.3	459.4 ± 1.3
2100	453.3 ± 2.4	464.2 ± 1.6	464.0 ± 1.6
2300	460.8 ± 2.9	473.0 ± 2.1	472.1 ± 2.1
2500	474.0 ± 3.8	486.4 ± 3.1	485.2 ± 3.1
2700	499.1 ± 6.0	511.1 ± 5.4	508.0 ± 5.4
2900	549.9 ± 13.0	549.9 ± 13.0	549.9 ± 13.0

Table 10: $|C_E|$ results (in ppb) and statistical uncertainties as a function of positron energy (in MeV). The first column ("bin result") shows $|C_E|$ recovered from each 200-MeV energy bin, whose lower energy is indicated. The second column ("threshold result") shows $|C_E|$ recovered from positrons between the indicated energy threshold and the maximum 3100 MeV. The third column ("avg. bin result") shows the statistics-weighted average of the energy-binned $|C_E|$ results corresponding to the same threshold, demonstrating good agreement.

7.8 Frequency-time correlation

TBD.

7.9 Field index

To be included (see other document).

7.10 Combination

To combine the systematic uncertainties, we must consider the correlations that may exist among the various sources. For example, it is likely that the uncertainty due to the background fit function depends on the chosen start time t_s, because the start time influences the background of the cosine transform.

Given the large number of systematic considerations listed throughout this section, due to computational constraints we estimate the effect of these correlations by averaging the results of the two extreme cases—no correlation, where the systematic uncertainties are added in quadrature; and full correlation, where the systematic uncertainties are added linearly. Furthermore, we restrict this combination scheme to the systematic uncertainties which are conceivably likely to be correlated. In particular, we apply this estimation to the parameters of the Fourier method, including the reference time t_0, start time t_s, end time t_m, frequency bin width, background definition threshold, and background removal threshold. These combinations are tabulated in Table 11. Once we obtain a combined uncertainty estimate for these parameters, the remaining sources of systematic uncertainty (i.e. quad alignment/voltage, field index, and momentum-time correlation) are assumed to be uncorrelated. These final systematic uncertainty combinations are tabulated in Table 12.

60Hour

source	σ_{x_e} (mm)	σ_σ (mm)	σ_{C_E} (ppb)
bkgd. fit	0.01	0.00	0.4
start time	0.02	0.02	2.1
end time	0.01	0.02	1.0
freq. bin	0.02	0.01	1.6
bkgd. def.	0.04	0.05	4.3
bkgd. rem.	0.01	0.02	1.9
quad. sum	0.06	0.07	6.1
linear sum	0.12	0.14	13.3
average	0.09	0.10	9.7

9Day

source	σ_{x_e} (mm)	σ_σ (mm)	σ_{C_E} (ppb)
bkgd. fit	0.04	0.01	2.8
start time	0.03	0.03	3.8
end time	0.01	0.01	0.9
freq. bin	0.02	0.01	1.9
bkgd. def.	0.05	0.07	6.5
bkgd. rem.	0.02	0.04	3.8
quad. sum	0.08	0.09	9.1
linear sum	0.17	0.17	19.7
average	0.12	0.13	14.4

EndGame

source	σ_{x_e} (mm)	σ_σ (mm)	σ_{C_E} (ppb)
bkgd. fit	0.02	0.00	0.6
start time	0.01	0.01	0.8
end time	0.01	0.01	0.8
freq. bin	0.01	0.01	0.4
bkgd. def.	0.06	0.07	2.1
bkgd. rem.	0.01	0.01	0.5
quad. sum	0.07	0.07	2.5
linear sum	0.12	0.11	5.2
average	0.09	0.09	3.9

HighKick

source	σ_{x_e} (mm)	σ_σ (mm)	σ_{C_E} (ppb)
bkgd. fit	0.07	0.01	4.0
start time	0.03	0.03	3.1
end time	0.01	0.02	1.1
freq. bin	0.01	0.01	1.3
bkgd. def.	0.05	0.06	6.5
bkgd. rem.	0.01	0.02	2.2
quad. sum	0.09	0.07	8.7
linear sum	0.18	0.15	18.2
average	0.14	0.11	13.4

Table 11: Uncertainties in x_e, σ, and C_E due to Fourier method parameters. To estimate correlations, these uncertainties are added both in quadrature and linearly, with the average of the two cases taken as the overall uncertainty from these sources. These results are then added in quadrature with the remaining sources of systematic uncertainty.

60Hour

source	σ_{x_e} (mm)	σ_σ (mm)	σ_{C_E} (ppb)
Fourier method parameters	0.09	0.10	9.7
quadrupole alignment/voltage	—	—	8.7
momentum-time correlation	0.55	0.35	50
field index	—	—	1.7
quadrature sum	0.57	0.37	52.3

9Day

source	σ_{x_e} (mm)	σ_σ (mm)	σ_{C_E} (ppb)
Fourier method parameters	0.12	0.13	14.4
quadrupole alignment/voltage	—	—	8.7
momentum-time correlation	0.66	0.34	63
field index	—	—	1.7
quadrature sum	0.69	0.37	66.4

EndGame

source	σ_{x_e} (mm)	σ_σ (mm)	σ_{C_E} (ppb)
Fourier method parameters	0.09	0.09	3.9
quadrupole alignment/voltage	—	—	8.7
momentum-time correlation	0.27	0.23	30
field index	—	—	4.0
quadrature sum	0.31	0.25	32.8

HighKick

source	σ_{x_e} (mm)	σ_σ (mm)	σ_{C_E} (ppb)
Fourier method parameters	0.14	0.11	13.4
quadrupole alignment/voltage	—	—	8.7
momentum-time correlation	0.61	0.34	52
field index	—	—	1.5
quadrature sum	0.64	0.36	55.5

Table 12: Combination of systematic uncertainties in x_e, σ, and C_E.

8 Conclusion

The final results and overall uncertainties are tabulated in Table 13.

Low Threshold
(results from 500 MeV threshold)

dataset	x_e (mm)	σ (mm)	C_E (ppb)
60Hour	$6.03 \pm (0.57)_{\mathrm{syst}} \pm (0.008)_{\mathrm{stat}}$	$9.20 \pm (0.37)_{\mathrm{syst}} \pm (0.007)_{\mathrm{stat}}$	$-459 \pm (52.3)_{\mathrm{syst}} \pm (0.60)_{\mathrm{stat}}$
9Day	$6.26 \pm (0.69)_{\mathrm{syst}} \pm (0.006)_{\mathrm{stat}}$	$9.19 \pm (0.37)_{\mathrm{syst}} \pm (0.005)_{\mathrm{stat}}$	$-515 \pm (66.4)_{\mathrm{syst}} \pm (0.54)_{\mathrm{stat}}$
EndGame	$6.60 \pm (0.31)_{\mathrm{syst}} \pm (0.003)_{\mathrm{stat}}$	$8.88 \pm (0.25)_{\mathrm{syst}} \pm (0.003)_{\mathrm{stat}}$	$-461 \pm (32.8)_{\mathrm{syst}} \pm (0.23)_{\mathrm{stat}}$
HighKick	$4.77 \pm (0.64)_{\mathrm{syst}} \pm (0.008)_{\mathrm{stat}}$	$9.19 \pm (0.36)_{\mathrm{syst}} \pm (0.007)_{\mathrm{stat}}$	$-446 \pm (55.5)_{\mathrm{syst}} \pm (0.64)_{\mathrm{stat}}$

High Threshold
(results from 1700 MeV threshold)

dataset	x_e (mm)	σ (mm)	C_E (ppb)
60Hour	$6.14 \pm (0.57)_{\mathrm{syst}} \pm (0.014)_{\mathrm{stat}}$	$9.23 \pm (0.37)_{\mathrm{syst}} \pm (0.012)_{\mathrm{stat}}$	$-466 \pm (52.3)_{\mathrm{syst}} \pm (1.04)_{\mathrm{stat}}$
9Day	$6.40 \pm (0.69)_{\mathrm{syst}} \pm (0.010)_{\mathrm{stat}}$	$9.23 \pm (0.37)_{\mathrm{syst}} \pm (0.009)_{\mathrm{stat}}$	$-525 \pm (66.4)_{\mathrm{syst}} \pm (0.94)_{\mathrm{stat}}$
EndGame	$6.73 \pm (0.31)_{\mathrm{syst}} \pm (0.005)_{\mathrm{stat}}$	$8.91 \pm (0.25)_{\mathrm{syst}} \pm (0.006)_{\mathrm{stat}}$	$-469 \pm (32.8)_{\mathrm{syst}} \pm (0.39)_{\mathrm{stat}}$
HighKick	$4.95 \pm (0.64)_{\mathrm{syst}} \pm (0.013)_{\mathrm{stat}}$	$9.22 \pm (0.36)_{\mathrm{syst}} \pm (0.011)_{\mathrm{stat}}$	$-456 \pm (55.5)_{\mathrm{syst}} \pm (1.10)_{\mathrm{stat}}$

Asymmetry Weighting
(asymmetry-weighted averages from energy-binned results above 1000 MeV)

dataset	x_e (mm)	σ (mm)	C_E (ppb)
60Hour	$6.15 \pm (0.57)_{\mathrm{syst}} \pm (0.012)_{\mathrm{stat}}$	$9.23 \pm (0.37)_{\mathrm{syst}} \pm (0.010)_{\mathrm{stat}}$	$-466 \pm (52.3)_{\mathrm{syst}} \pm (0.92)_{\mathrm{stat}}$
9Day	$6.41 \pm (0.69)_{\mathrm{syst}} \pm (0.009)_{\mathrm{stat}}$	$9.23 \pm (0.37)_{\mathrm{syst}} \pm (0.008)_{\mathrm{stat}}$	$-526 \pm (66.4)_{\mathrm{syst}} \pm (0.83)_{\mathrm{stat}}$
EndGame	$6.73 \pm (0.31)_{\mathrm{syst}} \pm (0.005)_{\mathrm{stat}}$	$8.91 \pm (0.25)_{\mathrm{syst}} \pm (0.005)_{\mathrm{stat}}$	$-469 \pm (32.8)_{\mathrm{syst}} \pm (0.35)_{\mathrm{stat}}$
HighKick	$4.95 \pm (0.64)_{\mathrm{syst}} \pm (0.012)_{\mathrm{stat}}$	$9.23 \pm (0.36)_{\mathrm{syst}} \pm (0.010)_{\mathrm{stat}}$	$-457 \pm (55.5)_{\mathrm{syst}} \pm (0.97)_{\mathrm{stat}}$

Table 13: Final results of the fast rotation analysis using the Fourier method, for three different positron energy weighting schemes. The systematic uncertainties have been estimated using a 1500-MeV threshold.

References

[1] A. Chapelain, J. Fagin, D. Rubin, D. Seleznev, *Cornell fast rotation Fourier method*, GM2-doc-18901

[2] A. Chapelain, J. Fagin, D. Rubin, D. Seleznev, *Performance study of the Cornell fast rotation Fourier analysis with toy Monte Carlo simulations*, GM2-doc-19132

[3] A. Chapelain, D. Rubin, D. Seleznev, *Extraction of the Muon Beam Frequency Distribution via the Fourier Analysis of the Fast Rotation Signal*, E989 note 130, GM2-doc-9701

[4] A. Chapelain, J. Fagin, D. Rubin, D. Seleznev, *On the background correction of the Cornell fast rotation Fourier method*, GM2-doc-19225

[5] A. Chapelain, J. Fagin, D. Rubin, D. Seleznev, *Cornell fast rotation Fourier analysis user guide*, GM2-doc-18460

[6] See Production Run–1 data wiki

[7] A. Fienberg, *Global T0 study*, GM2-doc-18964

[8] See 'TMC #1' in: GM2-doc-13759

[9] See 'TMC #3' in: GM2-doc-13759